

Article

Design and Testing of a Small-Scale Composting Facility for Sheep Manure Utilizing Aeration and Thermal Treatment

Jian Wang ^{1,2,*} , Kailin Ren ^{1,2,3} and Longfei Zhang ^{1,2}

¹ College of Mechanical and Electrical Engineering, Inner Mongolia Agricultural University, Hohhot 010018, China; m17362908182@163.com (K.R.); 18804936332@163.com (L.Z.)

² Inner Mongolia Engineering Research Center of Intelligent Equipment for the Entire Process of Forage and Feed Production, Hohhot 010018, China

³ Advanced Manufacturing College, Nanchang University, Nanchang 330031, China

* Correspondence: wj115@imau.edu.cn; Tel.: +86-159-4947-4869

Abstract: Inner Mongolia has the largest sheep population among China's provinces, resulting in the production of a substantial amount of sheep manure. If left untreated, this manure can contribute to environmental pollution. However, sheep manure serves a dual purpose: it can be both a pollutant and a valuable source of organic fertilizer. Consequently, there is an urgent need to address the environmental issues arising from manure accumulation and its unused status. In this paper, a viable solution is proposed: the conversion of manure into fertilizer through a composting unit incorporating high-temperature aerobic fermentation technology. This unit, tailored for small farms and individual farmers, integrates critical functions such as ventilation, heating, and turning. Additionally, it boasts excellent thermal insulation, enhancing composting efficiency and enabling precise control over fermentation conditions. This design mitigates heat loss and accelerates maturation, addressing common challenges in traditional composting. The design process encompassed both equipment construction and control systems, with a primary focus on compost fermentation and aeration heating. The components were carefully designed or selected based on theoretical analysis and subsequently validated using simulation software, including EDEM and Fluent. The control system seamlessly integrates a touch screen interface, PLC programming, and control circuits to manage air pumps and electric heaters in response to changes in temperature and oxygen concentration. Furthermore, it controls the motors during the recovery phase. A comprehensive performance evaluation was conducted, revealing notable improvements. Under artificially heated conditions, the maximum temperature of the compost increased by approximately 20 °C, the composting cycle was reduced by roughly 4 days, and the seed germination index (GI) rose by about 9% when compared to natural fermentation. Thus, this device significantly accelerates composting and improves fertilizer quality by increasing the decomposition rate.

Keywords: livestock manure; compost fermentation; organic fertilizer; composting trials; sustainable development



Citation: Wang, J.; Ren, K.; Zhang, L. Design and Testing of a Small-Scale Composting Facility for Sheep Manure Utilizing Aeration and Thermal Treatment. *Agriculture* **2024**, *14*, 2070. <https://doi.org/10.3390/agriculture14112070>

Academic Editor: Wenbing Zhou

Received: 8 October 2024

Revised: 14 November 2024

Accepted: 15 November 2024

Published: 18 November 2024



Copyright: © 2024 by the authors. Licensee MDPI, Basel, Switzerland. This article is an open access article distributed under the terms and conditions of the Creative Commons Attribution (CC BY) license (<https://creativecommons.org/licenses/by/4.0/>).

1. Introduction

China, a leading nation in agriculture and animal husbandry, has steadily moved its livestock and farming sectors toward large-scale operations and intensification in response to population increase [1–5]. However, the inadequate utilization and ineffective management of livestock and poultry manure have increasingly complicated rural ecological management [6–12]. Incorrect management results in environmental damage, and livestock manure is still underutilized as a renewable resource and source of organic fertilizer [13–23]. In order to address these concerns, safe treatment and resource use methods are crucial [24–28]. While modern composting equipment and high-temperature aerobic fermentation technology have the potential to improve manure treatment efficiency, reduce environmental pollution, and enhance organic fertilizer production, further research

and comparative analysis are necessary to validate these improvements over traditional methods [9,29–38].

Several academics have studied composting equipment with the goal of optimizing the form and function of the apparatus to increase composting efficiency and fermentation process controllability [39–46]. For instance, real-time sampling and detection, humidity and oxygen concentration management, and other features were included in the design of an aerobic composting unit for organic waste to improve control over fermentation conditions. Equipment for composting animal dung that uses heat exchangers and biofilters for heat recovery and odour removal is another advancement. In order to accelerate redox processes, raise composting temperatures quickly, and shorten the composting cycle, an apparatus for electrochemically assisting the composting of organic solid waste was also developed. When Chattip Prommuak et al. evaluated various compost stirring device mounting configurations, they discovered that horizontal stirring devices were more successful in promoting compost–air interaction [47]. In addition, Jonas Schneider et al. investigated operating circumstances at high fill levels, assessed compost mixing performance, and adjusted the parameters of a drum composting reactor [48].

According to previous research, the primary objectives of recent advancements in composting equipment are to improve the mixing process, optimize fermentation conditions, and minimize heat loss. Despite these developments, issues such as poor heat retention, ineffective mixing, and suboptimal equipment performance remain. Additionally, improving the accuracy of humidity and oxygen control is essential for a successful and manageable composting process. This study aims to develop composting equipment that integrates heating, rotating, aeration, and heat preservation functions to address inefficiencies in traditional composting methods. The design aims to shorten the composting cycle, improve decomposition, and accelerate fermentation by optimizing control over fermentation conditions and efficiency. It is anticipated that this integrated multifunctional design will provide fresh perspectives and answers for the ongoing advancement of composting machinery.

2. Design and Installation of Composting Equipment

2.1. Theoretical Analysis and Structural Design of Fermentation Silos

2.1.1. Target Compost Volume

During the design of the main structure of the fermentation silo, the internal volume of the fermenter was established at approximately 200 L ($V_{\text{canister}} \approx 200$ L) based on detailed analysis and consultation with the manufacturer.

A height-to-diameter ratio of the fermenter greater than 2 enhances the composting effect and reduces heat loss [16]. Therefore, the height and diameter of the fermentation chamber are configured to meet the following inequalities:

$$\frac{h_{\text{canister}}}{d_{\text{canister}}} > 2 \quad (1)$$

where h_{canister} is the internal height of the fermenter, m, and d_{canister} is the internal diameter of the fermenter, m.

The formula for the volume of a cylinder is

$$V = \pi r^2 \times h = \frac{1}{4} \pi d^2 \times h \quad (2)$$

where V is volume, m^3 ; r is radius, m; d is diameter, m; and h is height, m.

Substituting Equation (1) into Equation (2) yields the inequality relating the inner diameter h_{canister} and the internal volume d_{canister} of the fermenter:

$$d_{\text{canister}} < \sqrt[3]{\frac{2V_{\text{canister}}}{\pi}} \quad (3)$$

It is known that $V_{\text{canister}} = 200 \text{ L}$, which is substituted into Equation (3), and can be obtained as $d_{\text{canister}} < 0.503 \text{ m} = 503 \text{ mm}$. Combined with the actual processing conditions and the design requirements of the fermentation silo, the final determination of the fermenter internal diameter $d_{\text{canister}} = 500 \text{ mm}$. According to Equation (2), the corresponding internal height of the fermenter can be obtained as

$$h_{\text{canister}} = \frac{4V_{\text{canister}}}{\pi d_{\text{canister}}^2} = \frac{4 \times 0.2}{\pi \times 0.5^2} \text{ m} \approx 1.019 \text{ m} = 1019 \text{ mm}$$

During fermentation, gases such as ammonia, methane, hydrogen sulphide, and carbon dioxide are generated. Approximately 30% to 40% of the internal volume of the fermenter should be reserved for the temporary storage of these gases, while the heap should occupy 60% to 70% of the space [16]. In this study, the heap was designed to occupy 65% of the fermenter's internal space. Consequently, the volume occupied by the heap, $V_{\text{canister}} = 0.13 \text{ m}^3 = 130 \text{ L}$, can be determined. The diameter of the heap is assumed to be the same as the inner diameter of the fermenter, $d_{\text{canister}} = 500 \text{ mm}$, and the height of the heap can be calculated accordingly.

$$h_{\text{canister}} = \frac{4V_{\text{canister}}}{\pi d_{\text{canister}}^2} = \frac{4 \times 0.13}{\pi \times 0.5^2} \text{ m} \approx 0.662 \text{ m} = 662 \text{ mm}$$

Based on the calculation of the volume of the pile, the mass of the pile can be found by referring to Equation (4).

$$V = \frac{m}{\rho} \quad (4)$$

where V is the volume, m^3 ; m is the mass, kg ; and ρ is the density, kg/m^3 .

Sheep manure and maize stover were used as raw materials in this composting trial. The small amount of chopped maize stover added had a negligible effect on the total compost volume. During the composting process, sheep manure accumulates loosely, creating large porosity, which justifies the use of packing density for mass-to-volume conversion. The relevant literature indicates that the stacking density of sheep manure is $\rho_{\text{sheep's manure}} \approx 492.1 \text{ kg}/\text{m}^3$, which allows for the calculation of the heap material's mass, $m_{\text{stackers}} \approx 64 \text{ kg}$ [16]. Based on these calculations, the target composting volume for this equipment is approximately 64 kg.

2.1.2. Aeration Required for the Stack

Using high-temperature aerobic fermentation technology, the composting equipment's heating system quickly initiates the thermophilic phase while maintaining an ideal temperature range of 55 °C to 65 °C. Studies have shown that this temperature range is the most active for thermophilic bacteria, which greatly increases the effectiveness of fermentation and inactivates pathogens [43–45]. Compost decomposition slows down and becomes less effective below 50 °C; helpful bacteria may be injured by temperatures over 70 °C, thereby upsetting the fermentation process. Thus, it is essential to keep the temperature between 55 °C and 65 °C in order to speed up the composting process.

Using a hot-air unit, the goal temperature for the high-temperature stage was increased to around 65 °C in this investigation. The hot air was adjusted to 80 °C to enhance heat transfer efficiency and account for heat loss.

$$\phi_a = \frac{1}{4} \pi d^2 \cdot v_a \quad (5)$$

$$v_a = -\frac{\kappa}{\mu} \cdot \frac{\Delta P}{H} \quad (6)$$

where ϕ_a is the amount of ventilation, m^3/h ; d is the diameter of the cross-section through which the air flows, m ; v_a is the air velocity through the material, m/h ; κ is the material

gas permeability, m^2 ; μ is the aerodynamic viscosity coefficient, $kg/m \cdot h$; ΔP is the air pressure difference along the height of the material itself, $kg/m \cdot h^2$; and H is the height of the material, m.

A ventilation pipe at the bottom of the fermenter allows hot air to rise through the pile, maximizing heating and enhancing heat transmission. The beginning temperature of the pile is considered to be $15^\circ C$, with a goal heating temperature of $65^\circ C$ to determine the ventilation needs. The air temperature at the top is thought to be equivalent to the pile temperature, i.e., it rises as the pile warms up, while the air temperature at the bottom is fixed at $80^\circ C$. The air pressure differential ΔP at the material height is given as follows in Equation (6).

$$\Delta P = (\rho_0 - \rho)gH \times 3600^2 \quad (7)$$

where ρ_0 is the air density at the bottom of the material (kg/m^3), ρ is the air density at the top of the material (kg/m^3), g is the acceleration due to gravity (m/s^2), and H is the height of the material (m).

As the air temperature at the top of the pile increases, the pressure difference ΔP between it and the air at the bottom gradually decreases. Therefore, the average pressure difference is used in the calculation and substituted into the relevant equation. Studies have shown that air density ρ varies with air temperature T [49]. The relationship between the two at standard atmospheric pressure can be expressed as follows:

$$\rho = 1.158 \times 10^{-5} \times (T - 273.15)^2 - 0.004573 \times (T - 273.15) + 1.292 \quad (8)$$

where ρ is the air density, kg/m^3 , and T is the air temperature, K.

In engineering thermodynamics, the numerical relationship between degrees Celsius ($^\circ C$) and Kelvin (K) is given by

$$T_2 = T_1 + 273.15 \quad (9)$$

Therefore, the air densities at $80^\circ C$, $65^\circ C$, and $15^\circ C$ are denoted as $\rho_{80^\circ C} \approx 1.000 kg/m^3$, $\rho_{65^\circ C} \approx 1.044 kg/m^3$, and $\rho_{15^\circ C} \approx 1.226 kg/m^3$, respectively. By knowing the height of the material $H = 662 mm$ and the acceleration of gravity $g = 9.8 m/s^2$, the maximum and minimum air pressure differences can be calculated as $\Delta P_{max} \approx -1.900 \times 10^7 kg/m \cdot h^2$ and $\Delta P_{min} \approx -3.699 \times 10^6 kg/m \cdot h^2$, respectively, with the mean value denoted as $\Delta P \approx -1.135 \times 10^7 kg/m \cdot h^2$.

Similar to air density, the aerodynamic viscosity coefficient varies with air temperature T [49]. The relationship between the aerodynamic viscosity coefficient and air temperature at standard atmospheric pressure can be expressed as follows:

$$\mu = 1.78 \times 10^{-4} \times (T - 273.15) + 0.06171 \quad (10)$$

where μ is the aerodynamic viscosity coefficient and T is the air temperature, K.

The maximum and minimum aerodynamic viscosity coefficients are denoted as $\mu_{max} \approx 0.076 kg/m \cdot h$ and $\mu_{min} \approx 0.064 kg/m \cdot h$, respectively. Since the required airflow rate v_a corresponds to the airflow rate inside the heap, the average of the two coefficients is taken to calculate the average aerodynamic viscosity coefficient.

As the temperature of the pile material rises, its porosity decreases, resulting in an increase in pile density and a reduction in gas permeability [16]. Additionally, the particle size, shape, and surface properties of the material change with temperature, further influencing gas permeability. Gas permeability can be modelled using the Ergon formula.

$$\kappa = \frac{d_p^2 \times \varepsilon^3}{150 K(1 - \varepsilon)^2} \quad (11)$$

where κ is the material gas permeability, m^2 ; d_p is the material particle diameter, m; ε is the material permeable void rate, %; and K is the material particle shape factor.

Due to the sloughing phenomenon of sheep manure raw material, it is necessary to crush the raw material appropriately before composting. The overall particle size should be approximately 5 mm to 8 mm. To calculate the gas permeability of the material, sheep manure particles are approximated as ellipsoidal or spherical. The average diameter of the particles is taken to be 6 mm, denoted as $d_p = 6$ mm.

The relevant literature [50] suggests that for the high-temperature aerobic composting of livestock manure, the ideal void ratio of the pile ranges from 85% to 90%, with the free-air void ratio typically between 30% and 36% (where free-air void refers to the portion of the total void not occupied by moisture). In this study, the permeable void ratio of goat manure is taken as 33%, denoted as $\varepsilon = 33\%$.

The material particle shape factor is defined as a dimensionless quantity used to characterize the shape of particles, with these quantities collectively referred to as the shape factor. This involves a geometric or physical quantity proportional to a specified particle size d_j and related sub-proportionalities. The particle shape factor, particularly in terms of volume, can be expressed using the following formula:

$$\varphi_{V,j} = \frac{V}{d_j^3} \quad (12)$$

where $\varphi_{V,j}$ is the volume shape factor, V is the particle volume (m), and d_j is the specified particle size (m).

For spherical particles, the volume shape factor is $\varphi_{V,j} = \frac{\pi}{6}$; for cubic particles, it is $\varphi_{V,j} = 1$. Since sheep manure particles are approximated as ellipsoidal or spherical in this study, the shape factor for sheep manure particles is taken as $K = \frac{\pi}{6}$.

Substituting each of the above parameters into Equation (11) yields the gas permeability of the pile, $\kappa \approx 3.670 \times 10^{-8} \text{ m}^2$. Given the known height of the pile, $H = 662$ mm, and substituting the results of each parameter into Equation (6), we obtain the airflow rate inside the pile: $v_a \approx 8.989 \text{ m/h} \approx 2.497 \times 10^{-3} \text{ m/s}$. To calculate the required aeration for the pile ϕ_a , the diameter of the cross-section through which the air flows is the diameter of the pile, denoted as $\phi_a \approx 1.765 \text{ m}^3/\text{h} \approx 29.417 \text{ L/min}$. Therefore, the airflow rate of the pile is calculated based on the diameter of the pile. Considering the control of the actual aeration volume and the subsequent selection of air pumps, it was determined that the required aeration volume should be at least 30 L/min under the target composting volume specified in this study. The results of this calculation can be used for subsequent heat balance analysis and for selecting appropriate air pumps, providing a reference for future studies.

2.1.3. Analysis of the Need for Insulation and Subsequent Design

Relevant research [51] shows that the side walls of a cylindrical composting reactor contribute significantly more to heat loss than any other component. Because heat transfers throughout the composting process, the fermenter's bottom and side wall surfaces, which are in direct contact with the compost, lose more heat. In order to confirm the need for an insulation layer, further analysis is performed on the heat dissipation of the fermenter's side and bottom surfaces, assuming that it is a single-layer construction.

In these circumstances, examining the heat transfer between the outside air and the side and bottom surfaces of the fermenter is necessary in order to analyse the heat loss caused by the material pile through the wall. The fermenter and the material pile are positioned as a cylinder in this part, and the impact of the intake and outflow ports' shapes is disregarded. A cylindrical reference is used in the appropriate calculations for parameter selection. According to Newton's law of cooling, the heat flow of convective heat transfer between a fluid and a solid surface is proportional to the temperature difference between them. It is expressed as follows:

$$q = h \cdot (T_{\text{solid}} - T_{\text{fluids}}) \quad (13)$$

$$Q = h \cdot (T_{\text{solid}} - T_{\text{fluids}}) \cdot S = q \cdot S \quad (14)$$

where q is the unit area of solid surface and fluid heat exchanged in the unit time, also known as heat flow density, W/m^2 ; Q is the unit time of a fixed area of heat transfer, W ; h is the surface convective heat transfer coefficient, $W/m^2 \cdot K$; S is the contact area, m^2 ; T_{solid} is the solid surface temperature, K ; and T_{fluids} is the fluid temperature, K .

Referring to the calculation methods of related research, the surface convective heat transfer coefficient expressions for the side and bottom surfaces of the fermenter under the aforementioned conditions are as follows, respectively [49]:

$$h_{\text{lateral}} = \frac{\lambda}{H} \cdot Nu_{\text{lateral}} \quad (15)$$

$$h_{\text{bottom}} = \frac{\lambda}{0.9d} \cdot Nu_{\text{bottom}} \quad (16)$$

where λ is the air thermal conductivity, $W/m \cdot K$; H is the height of the material in the fermenter, m ; d is the inner diameter of the fermenter, m ; and Nu is the Nusselt criterion number (air free convection Nusselt number), which expresses the strength of convective heat transfer.

The specific expressions of the Nusselt number are as follows:

$$Nu_{\text{lateral}} = 0.59(Gr_{\text{lateral}} \cdot Pr)^{0.25} \quad (17)$$

$$Nu_{\text{bottom}} = 0.54(Gr_{\text{bottom}} \cdot Pr)^{0.25} \quad (18)$$

where Gr is the Grashof number, representing the ratio of buoyancy to viscous forces in natural convection, and Pr is the Prandtl number, representing the ratio of a fluid's ability to transfer momentum to its ability to transfer heat.

The Grashof number can be specifically expressed as follows:

$$Gr_{\text{lateral}} = \frac{2g(T_s - T_a)H^3}{(T_s + T_a)\nu^2} \quad (19)$$

$$Gr_{\text{bottom}} = \frac{2g(T_s - T_a)(0.9d)^3}{(T_s + T_a)\nu^2} \quad (20)$$

where g is the gravitational acceleration, m/s^2 ; T_s is the wall temperature of the fermenter, K ; T_a is the outside air temperature, K ; H is the height of the material in the fermenter, m ; d is the inner diameter of the fermenter, m ; and ν is the coefficient of kinematic viscosity of the air, m^2/s^2 .

The air kinematic viscosity coefficient ν can be expressed as the ratio of the kinetic viscosity coefficient μ to the fluid density ρ with the expression

$$\nu = \frac{\mu}{\rho} \quad (21)$$

where μ is the aerodynamic viscosity coefficient, $kg/m \cdot s$, and ρ is the air density, kg/m^3 .

Considering the outside air temperature as room temperature ($15^\circ C$), the kinetic viscosity coefficient of room-temperature air, $\mu \approx 1.778 \times 10^{-5} kg/m \cdot s$, can be obtained according to Equation (10); the density of room-temperature air $\rho \approx 1.226 kg/m^3$. The kinematic viscosity coefficient of room-temperature air $\nu \approx 1.450 \times 10^{-5} m^2/s$ can be obtained by substituting each parameter into Equation (21).

In this study, 304 stainless steel is used as the fermenter processing material. Due to the good thermal conductivity of metal materials, it can be assumed that the temperature of the fermenter wall surface is approximately equal to the temperature of the pile material.

According to previous findings, the temperature of the pile material is 65 °C, and thus, the temperature of the fermenter wall surface is also 65 °C. The acceleration of gravity is denoted as $g = 9.8 \text{ m/s}^2$, the height of the pile material in the fermenter as $H = 662 \text{ mm}$, and the inner diameter of the fermenter as $d = 500 \text{ mm}$. By substituting these parameters into Formulas (19) and (20), the Grashof numbers for the side and bottom surfaces of the fermenter are $Gr_{\text{lateral}} \approx 2.159 \times 10^9$ and $Gr_{\text{bottom}} \approx 6.782 \times 10^8$, respectively.

According to the relevant literature [51], the Prandtl number $Pr \approx 0.714$ and the thermal conductivity $\lambda \approx 0.025 \text{ W/m} \cdot \text{K}$ of room-temperature air at 1 standard atmospheric pressure. Substituting the Grashof number and Prandtl number into Equations (17) and (18), the Nusselt numbers of the side and bottom surfaces of the fermenter are $Nu_{\text{lateral}} \approx 116.907$ and $Nu_{\text{bottom}} \approx 80.105$. Substituting the thermal conductivity of the air λ and the Nusselt number into Equations (15) and (16), the convective coefficients of the surface heat transfer between the side and the bottom surfaces of the fermenter are $h_{\text{lateral}} \approx 4.415 \text{ W/m}^2 \cdot \text{K}$ and $h_{\text{bottom}} \approx 4.450 \text{ W/m}^2 \cdot \text{K}$.

Based on the commonly used size specifications of 304 stainless-steel plates in the current market and considering the actual requirements of the equipment, the wall thickness of the fermenter is determined to be 3 mm. Since the tank is approximated as a cylinder, the contact area of the fermenter sides and bottom, which are in direct contact with the pile, can be approximated as $S_{\text{lateral}} \approx 1.052 \text{ m}^2$ and $S_{\text{bottoms}} \approx 0.201 \text{ m}^2$, respectively, accounting for the wall thickness. By substituting these parameters into Equation (14), the heat transfer on the sides and bottom of the fermenter per unit time can be calculated as $Q_{\text{lateral}} \approx 232.229 \text{ W}$ and $Q_{\text{bottoms}} \approx 44.723 \text{ W}$, respectively, as shown below:

$$\frac{Q_{\text{lateral}} - Q_{\text{bottoms}}}{Q_{\text{lateral}}} \times 100\% = \frac{232.229 - 44.723}{232.229} \times 100\% \approx 80.721\%$$

The heat transmission from the fermenter's sides was around 80.721% more than from the bottom, according to our calculations, underscoring the real-world significance of adding insulation to the sides. This research enhanced the fermenter design by adding a double-layer structure akin to a silo to reduce heat loss. The insulating material used in the cavities between layers was a stiff polyurethane sponge that measured 50 mm in thickness. Standard criteria were used to estimate the thickness of the insulation layer.

2.1.4. Inlet and Outlet Design

Feeding and discharging openings are included in the side and bottom of the fermenter's structural construction to make handling materials easier while the composting machinery is in action. The inlet has an open-and-closed door and a sloping intake channel, which allow for simultaneous feeding and stirring to improve the effectiveness of mixing the compost and to reduce interference with the stirrer during feeding. The discharge port is positioned in the middle of the funnel-shaped fermenter bottom, which encourages the heap material to naturally descend. To link the discharge port's outer ring to the screw feeder's input port, a flange is welded there. The intake is around 400 mm in length and 200 mm in width overall. Its bottom slopes downward to allow the pile to naturally fall into the fermenter. The outlet's inner diameter is around 150 mm, and the flange has six holes for attachment.

2.1.5. Design of the Mixing Unit

The stirring mechanism of this composting equipment is a pneumatic stirrer, which is attached to a ventilation line at the air pump's air output. The heating box is linked to an additional ventilation pipe. This design makes it possible to integrate the stirring, heating, and ventilation processes, which streamlines the equipment's operation. Furthermore, the energy expenses of the composting equipment are considerably decreased by using a pneumatic stirrer. The main parts of a pneumatic stirrer are stirring blades, a revolving shaft, and a cylinder. The cylinder rotates two sets of stirring blades that are fixed at the

top and bottom of the spinning shaft. The operating parameters are outlined in Table 1 and the rotating shaft has a length of around 830 mm.

Table 1. Working parameters of pneumatic agitator.

Power (HP)	Speed (r/min)	Working Air Pressure (MPa)	Mixing Capacity (L)
0.5	50~2800	0.6~0.8	200

With reference to the pertinent literature, traditional stirring blades were refined to improve the heap's flow characteristics and guarantee more complete contact with hot air, which in turn increased the fermentation effect [50,51]. Three transverse main paddles and many oblique subsidiary paddles make up the upgraded mixing blades. Each of the three transverse major paddles is separated 120° away from the other by the main paddles, which are welded to the intermediate support component at a 45° angle to the axial direction of the rotating shaft. The three oblique sub-propellers are fixed and placed in parallel with each transverse main paddle, creating a 60° angle between each sub-propeller and the transverse main paddle. The intermediate support section is fastened to the spinning shaft with a set screw and has threaded holes on the side.

2.1.6. Design of the Pick-Up Device

At the fermenter's output, a reclamation mechanism is added to significantly increase the efficiency of reclaiming. The cycloid reducer and screw feeder make up the majority of this apparatus. The screw feeder's input end is fixed to the fermenter's discharge port via a flange, and its output end functions as the discharge port. The material may be moved from one end of the screw feeder to the other for discharge thanks to the cycloid reducer's driving of the screw belt shaft via a gear chain drive. The conveying pipe has an inner diameter of about 200 mm and a length of about 520 mm, while the screw feeder's inlet and outlet ends have an inner diameter of 150 mm. The single-phase, double-capacitor asynchronous motor in use has a reduction ratio of 1:59, as enforced by the cycloid reducer. Table 2 provides specifics on the operating parameters.

Table 2. Working parameters of motor.

Power (HP)	Speed (r/min)	Working Air Pressure (MPa)	Mixing Capacity (L)
0.5	50~2800	0.6~0.8	200

A Y-shaped tee connection creates two distinct ventilation lines when an air pump is used. Air is routed via one ventilation line to the heating box, which warms the air and uses the aeration pipework to distribute it into the fermenter. The other ventilation line is attached to a pneumatic stirrer, which powers the rotor shaft with the help of a cylinder. As a result, when choosing the right air pump, it is important to take the pile's aeration requirements and the stirrer's required operating air pressure into account.

In accordance with Section 2.1.2, the heap needs at least 30 L/min of aeration during the fermentation phase in order to reach the equipment's goal composting volume. At constant operating air pressure, the agitator's rotational speed increases with greater aeration volumes and is directly proportional to the gas flow rate. An air pump model that is widely accessible on the market was chosen based on these requirements. Its dimensions (L × W × H) are around 420 mm × 410 mm × 675 mm. The air pump's physical characteristics are seen in Figure 1, and Table 3 lists all of its operational specifications. The air pump's exhaust pressure and output volume both satisfy the pile's ventilation demands and the operating air pressure requirements of the pneumatic mixer.



Figure 1. Air pump (oil-free air compressor).

Table 3. Working parameters of air pump.

Product Model	Tank Volume (L)	Input Voltage (V)	Frequency (Hz)	Input Power (kW)	Exhaust Volume (L/min)	Rotation Speed (r/min)	Exhaust Pressure (MPa)
JYK35	35	220	50	0.8	65	1400	0.8

2.1.7. Structural Design of the Heating Box

The heating box has a rectangular shape, with internal dimensions designed according to the structural specifications of the fermenter: 500 mm × 350 mm × 300 mm (length × width × height). Then, the volume of air inside the box can be obtained:

$$V_{air} = 0.053 \text{ m}^3$$

The heating box, made of 304 stainless steel with a wall thickness of 3 mm, consists of two main parts: the top cover and the box body. An electric heating pipe is installed in the middle of the top cover. The box has air inlet and outlet ports on both sides, each connected to the inlet and outlet pipelines, respectively. Based on the structural dimensions of the heating box, the surface areas of the top, bottom, and sides can be calculated as follows:

$$S_{topmost} = S_{bottoms} = 0.175 \text{ m}^2$$

$$S_{lateral} = 0.510 \text{ m}^2$$

According to the above, further heat balance analysis of the air heating process is required so as to determine the power parameters of the electric heaters used to complete the selection of electric heaters.

2.1.8. Air Pump Selection

The air from the air pump is heated as it passes through the electric heater before entering the heating box. Although the air absorbs heat during this process, several forms of heat loss also occur. Consequently, in order to comprehend the heat transfer that occurs throughout the air heating process, a heat balance analysis must be carried out. This examination aids in determining the electric heater's proper power. The model and size of the heater may then be chosen based on the popular kinds of electric heaters that are available on the market. The following is the air heating process's heat balance equation:

$$q_{eht} = q_{ia} + q_{hc} + q_{ste} + q_{else} \quad (22)$$

where q_{eht} is the heat released by the electric heater, kJ/h; q_{ia} is the heat absorbed by the air pump input air warming, kJ/h; q_{hc} is the heat conducted by the wall of the heating box, kJ/h; q_{ste} is the heat absorbed by the evaporation of moisture in the air, kJ/h; and q_{else} is the other forms of heat loss, kJ/h.

Assuming that the power of the electric heater is $P(W)$, the heat given off by the heater can be expressed as follows:

$$q_{eht} = 3.6 P \text{ kJ/h} \quad (23)$$

The heat absorbed by the warming of the air input to the air pump can be expressed as follows:

$$q_{ia} = c_{air} \cdot \rho_{air} \cdot \phi_{air} \cdot \Delta T_{air} \quad (24)$$

where c_{air} is the specific heat capacity of air, $\text{kJ/kg} \cdot \text{K}$; ρ_{air} is the density of air, kg/m^3 ; ϕ_{air} is the ventilation volume, m^3/h ; and ΔT_{air} is the air temperature change value, K .

From the aforementioned content, it is evident that the required ventilation rate for the material pile is at least 30 L/min. Therefore, the air output from the air pump in the heating box's ventilation circuit must meet this requirement, denoted as $\phi_{air} \approx 30 \text{ L/min} = 1.8 \text{ m}^3/\text{h}$. At a standard atmospheric pressure and a temperature of 15°C , the air density and specific heat capacity at constant pressure are $\rho_{air} = 1.226 \text{ kg/m}^3$ and $c_{air} = 1.005 \text{ kJ/kg} \cdot \text{K}$, respectively. The change in air temperature is denoted as $\Delta T_{air} = 65 \text{ K}$. By substituting these parameters into Equation (24), the heat absorbed by the air as it is heated by the air pump can be determined:

$$q_{ia} \approx 144.159 \text{ kJ/h}$$

The heat conducted through the walls of the heating box is expressed as follows:

$$q_{hc} = \lambda_{air} \cdot A \cdot \frac{\Delta T}{d} \quad (25)$$

where λ_{air} is the air thermal conductivity, $\text{W/m} \cdot \text{K}$; A is the contact area, m^2 ; ΔT is the temperature difference between the objects, K ; and d is the heat transfer distance, m .

Due to the good thermal conductivity of the stainless-steel wall, it can be considered that the wall temperature of the heating box is approximately equal to the internal temperature of the hot air, that is, $T_{wall} \approx T_{air}$; then, the maximum temperature difference between the wall of the heating box and the outside air $\Delta T_{\text{max}} = 65 \text{ K}$. As the difference between the two temperatures from 0 to 65 K is gradually increasing, take the average value for calculation. At 1 standard atmospheric pressure at room temperature, air thermal conductivity $\lambda_{air} = 0.025 \text{ W/m} \cdot \text{K}$; the heating box and the contact area of the outside air $A \approx 0.685 \text{ m}^2$. Due to the heating box wall thickness of $\delta = 3 \text{ mm}$, the wall of the heat transfer distance $d = 1.5 \text{ mm} = 0.0015 \text{ m}$. Substituting the above parameters into Formula (25), you can obtain the heating box wall heat conduction of

$$q_{hc} \approx 376.978 \text{ W} \approx 1357.122 \text{ kJ/h}$$

The heat absorbed by the evaporation of water in the air is expressed as

$$q_{ste} = \phi_{air} \cdot \rho_{air} \cdot \Delta x \cdot q_l \quad (26)$$

where ϕ_{air} is the ventilation volume, m^3/h ; ρ_{air} is the air density, kg/m^3 ; Δx is the net mass of water vapour in the air, kg/kg ; and q_l is the enthalpy of water vapour, kJ/kg .

By consulting relevant information, the air physical parameters calculator, and other computer-aided tools, it is found that when the air temperature is 15°C and humidity is 20% (in Inner Mongolia, for example), the net mass of water vapour in the air is about $\Delta x \approx 0.002 \text{ kg/kg}$. Similarly, the enthalpy of the water vapour is about $q_l \approx 20.4 \text{ kJ/kg}$. With the corresponding parameter substitution into Formula (26), the heat absorbed by the evaporation of water in the air can be obtained as

$$q_{ste} \approx 0.095 \text{ kJ/h}$$

In the actual air heating process, besides the aforementioned types of heat loss, there are also more complex forms of heat transfer. These include thermal radiation and heat dissipation at the ventilation duct connections. In this section on heat balance analysis, these are collectively referred to as "other forms of heat loss", denoted as q_{ste} .

Based on the results of the above calculations for each form of heat loss, combined with the heat balance Equation (22), it can be seen that

$$q_{eht} > q_{ia} + q_{hc} + q_{ste}$$

$$3.6P > 144.159 + 1357.122 + 0.095$$

Further, the power of the electric heater can be obtained as

$$P > 417 \text{ W}$$

In addition to the analysis of regularly used power requirements and kinds of electric heaters available on the market, a thorough analysis was given to various sources of heat loss during the heating process based on the findings of the calculations mentioned above. The type and characteristics of the electric heaters were chosen based on the design of the heating box's structural dimensions. The hot gas device's electric heater's ultimate power was determined to be 500 W. The chosen model is a 220 V dry-burning electric heater with a W-shaped finned structure. The electric heater's centre distance between the positive and negative poles is around 180 mm, and the tube body's diameter—including the fins—is roughly 24 mm.

2.1.9. Design of Ventilation Ducts

For ventilation, the composting factory uses 304 stainless-steel pipes and polyurethane hoses. The air pump outlet, heating box inlet, and agitator inlet are linked by polyurethane hoses, while the fermenter's aeration, venting, and heating box output are made of stainless-steel pipes. The nominal diameter of the stainless-steel pipes used in the piping system is 50 mm, and they are developed in accordance with the equipment structure. The heating box and fermentation tank are connected by an S-shaped pipe, and the deodorant device—which uses activated carbon to adsorb odours—is connected to the exhaust port of the fermentation tank by a straight pipe. A three-row diagonal downward sub-pipe design that ensures consistent hot air distribution and avoids clogs improves the aeration pipe.

2.2. Model Drawing and Simulation Analysis

The major component of the composting apparatus was developed, and a SolidWorks model was made based on calculations and theoretical analysis. This model may be used to replicate how the machinery operates or how the compost material is heated, allowing the viability of the idea to be confirmed. The equipment's construction and machining will be guided by the part drawings produced by the model.

2.2.1. Three-Dimensional Model of Composting Equipment

Four components make up the modelling of this composting equipment: the rack, the aeration and heating system, the control system, and the compost fermentation system. Fermentation tanks, agitators, feeding apparatuses, and deodorisation apparatuses make up the compost fermentation system, which also includes the fermentation silo. Air pumps, heating tanks, electric heating tubes, and ventilation pipes make up the aeration and heating system, which also contains a hot-air device. The control box, which consists mostly of a touch screen and programmable logic controllers, is part of the control system, along with sensors. The aluminium profiles, fasteners, and base plate make up the rack.

The models of the hot gas device and the fermentation bin were developed with reference to the structural design specifications included in Sections 2.1 and 2.2. The control box model was included, and the structural dimensions of the rack were calculated and modelled for assembly based on the installation locations of these components. Figure 2 displays the whole composting apparatus concept.

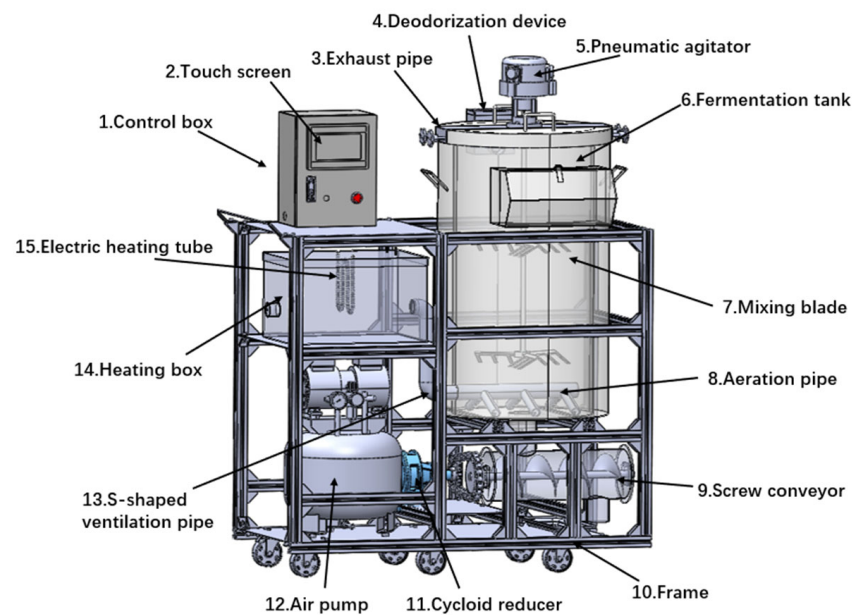


Figure 2. Three-dimensional model of composting equipment.

2.2.2. EDEM-Based Churning Analysis

The material mixing process during composting was simulated and analysed using EDEM2018 software, and the enhanced mixing blades' mixing performance was compared with that of conventional paddle and spiral belt blades. In order to make sure that the analysis correctly depicted the real mixing process, the model was reduced to its essential elements, which were the fermenter body, shaft, and mixing blades. The results confirmed the rationality of the improved blade design. Simplified models of the three types of blades in EDEM are shown in Figure 3.

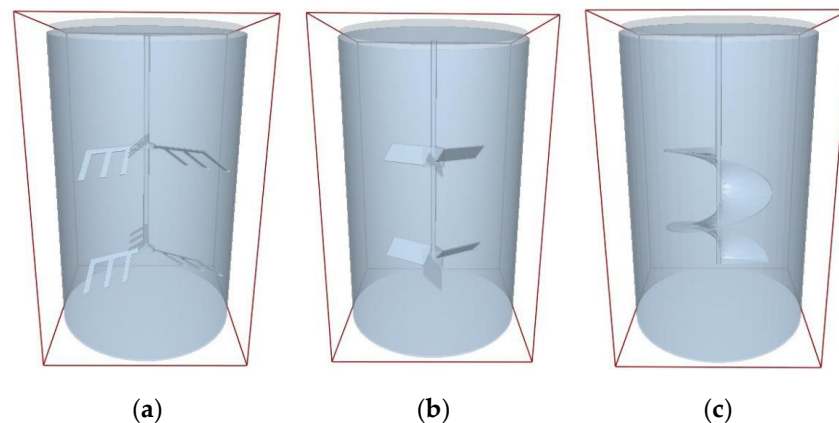


Figure 3. Simplified model of material mixing for simulation of EDEM. (a) Improved blade; (b) paddle blade; (c) ribbon blade.

Based on the simplified model, the simulation parameters and conditions for the compost mixing model with improved blades were established. Two types of sheep manure particles, each constituting 50% of the total particles, were modelled, while the effect of straw particles was neglected, the two types of particles are shown in Figure 4. The primary focus was on the flow characteristics of the sheep manure particles. The physical and geological properties of the particles were set according to values in the literature, and the interactions between wet particles and the geometry were simulated using the 'Hertz–Mindlin with JKR' model. The simulation ran for 10 s, with the time step and mesh parameters appropriately configured to ensure accurate results.

In the post-processing module of EDEM, particle velocity data were collected using a velocity sensor to compare particle motion and overall flow under different blade agitation types, allowing for an assessment of the agitation effect. The particle motion during the first 6.5 s of the simulation was selected for comparison and analysis of the performance of the three mixing blade types. The simulation results are presented in Figure 5.

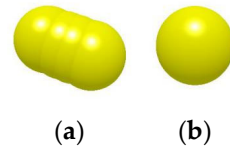


Figure 4. Model of sheep dung pellet. (a) Ellipsoid; (b) spherical.

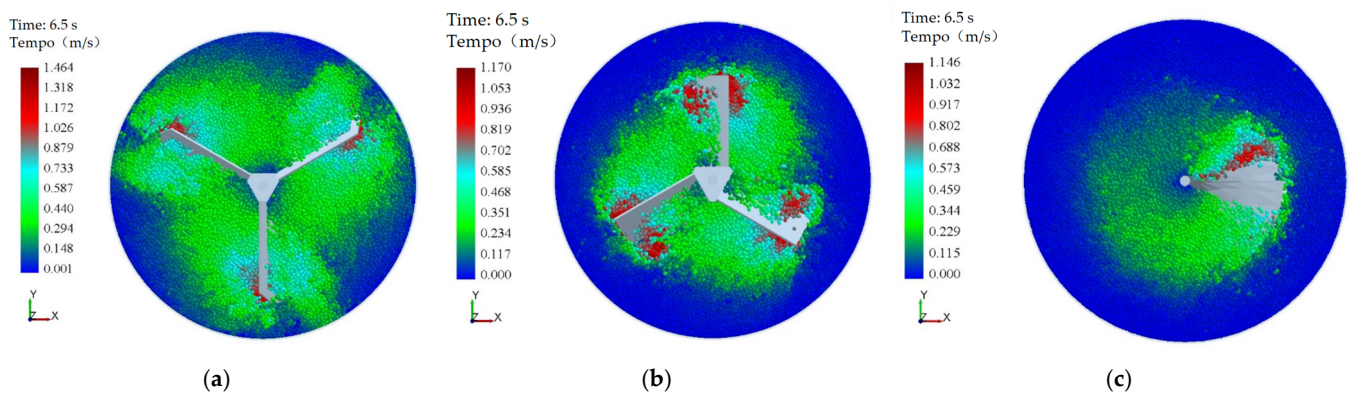


Figure 5. Motion speed image of particles at 6.5 s in simulation. (a) Agitation of improved blade; (b) agitation of paddle blade; (c) agitation of ribbon blade.

As shown in Figure 5, the particle movement speed under the improved blade stirring is significantly higher than in the other two cases, resulting in the best stirring effect on the material. The oblique sub-blade drives most particles within the blade sweeping area, with the particle speed at the blade tip reaching a relative maximum. Compared to the traditional blades, the improved blade demonstrates the best stirring effect on the peripheral compost, effectively enhancing the radial flow performance of the particles. This improvement allows the compost to make better contact with hot air, thereby enhancing the heating effect during actual composting. Additionally, the particle velocity vector diagram in Figure 6 further illustrates that particles at the leading edge of the blade move downward before rising along the leading edge due to the blade's motion. The secondary paddle increases the particle velocity at the trailing edge, driving peripheral particles through collisions. The synergistic action of the upper and lower blades creates a mutual flow between particles, thereby improving the mixer's stirring performance.

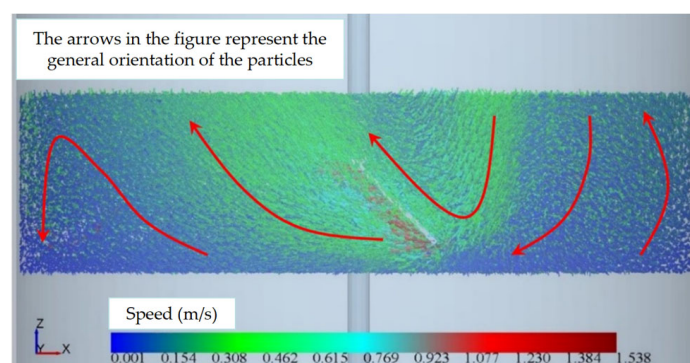


Figure 6. Improved blade-particle velocity vector.

A particle mass flow sensor is installed in the area between the two sets of mixing blades. This sensor collects data on the mass of particles flowing through the area per unit time, which indirectly indicates the number of particles passing through and their mobility within the heap under different types of blade agitation. Figure 7 shows the grid portion where the particle mass flow sensor is located.

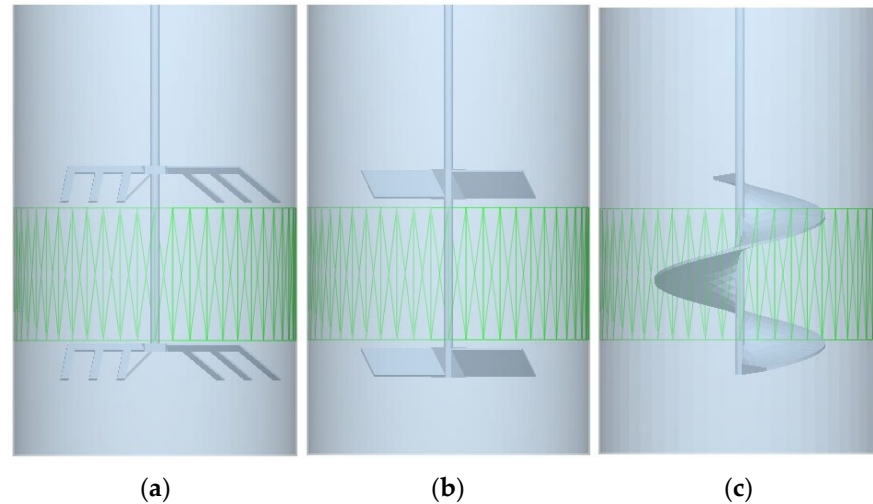


Figure 7. Schematic chart of particle mass flow sensor setup. (a) Model of improved blade; (b) model of paddle blade; (c) model of ribbon blade.

The agitation of the blades pushes the particles in the axial direction, and a higher frequency or number of particles indicates a higher mass flow rate. The line graph in Figure 8 shows the particle mass flow rate in this region for the three blades, with the values indicating the direction of particle flow and the flow rate per unit of time. The improved blades significantly improved the flow in the middle of the stockpile, with frequent and larger axial flows indicating better mixing. Overall, the improved blades enhanced the radial mixing performance and improved the axial flow compared to the conventional blades, which verified the feasibility and effectiveness of their design.

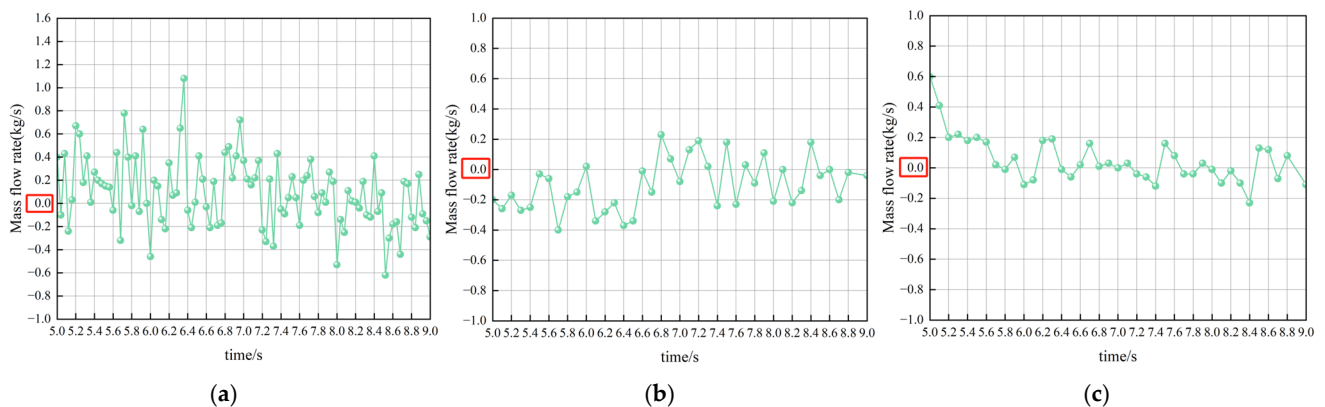


Figure 8. Broken line graph of particle mass flow in the corresponding areas of the three types of blades. (a) Mass flow of particles under the action of improved blades; (b) mass flow of particles under the action of paddle blades; (c) mass flow of particles under the action of ribbon blades.

2.2.3. Fluent-Based Analysis of Ventilation Heating

Fluent was used to simulate the aeration heating and stirring process during the high-temperature stage of composting to study and analyse the temperature changes in the compost. This simulation, combined with the aforementioned theoretical analysis and calculation results, helps to further understand the compost warming process and the required heating time,

providing theoretical guidance and a reference basis for subsequent composting tests. The simulation focuses on the compost fermentation and aeration heating processes. The compost equipment model was simplified before mesh division and solution calculation, retaining only key parts such as the main fermenter, rotor shaft, mixing blade, aeration pipeline, and exhaust pipeline. Other relevant parameters and conditions were set in Fluent to simulate the actual effects. As shown in Figure 9a, the simplified model meets the simulation needs while realistically reflecting the actual aeration heating and mixing process.

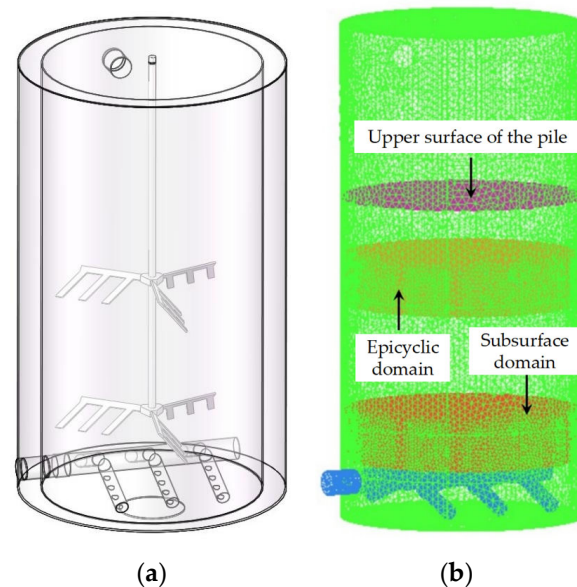


Figure 9. Simplified model and mesh model for simulation in Fluent. (a) Simplified model; (b) mesh model.

Based on the simplified model, ICEM was used for meshing to delete redundant structural surfaces and add boundary surfaces for setting boundary conditions, such as the upper surface of the pile and the upper and lower rotation domains (Figure 9b). The model was divided using unstructured meshing to improve the overall quality of the mesh. The results of the mesh quality check are shown in Figure 10, which indicates that all mesh quality values are greater than 0.2, meeting the basic requirements for Fluent simulation. Consequently, the mesh model can be imported into Fluent for solution calculation.

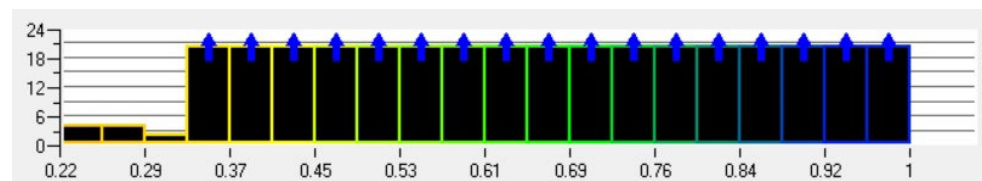


Figure 10. Inspection chart of mesh quality.

In this simulation, energy equations and a standard turbulence model are used for the calculation model, material properties and geometric characteristics are set, and the stirring effect of the mixing blade is simulated by fixed-axis uniform rotation. After completing the boundary conditions and mesh contact surface settings, the solver is initialized and calculated. The temperature change in the hot-air-heated heap was depicted by the profile temperature cloud (Figure 11), the initial temperature was 55 °C, the hot-air temperature was 80 °C, the simulation lasted for 30 min, and the compost temperature increased to about 59 °C. Combined with the practical requirements, the operating time of the hot-air unit can be estimated to be about 1 h and 15 min, which can be used as a reference for the time control of subsequent composting experiments.

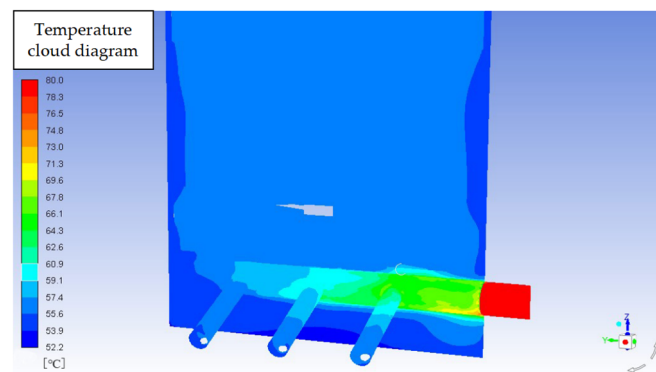


Figure 11. Temperature contour of the stacked material profile.

The installation of the components of the composting equipment is shown in Figure 12.

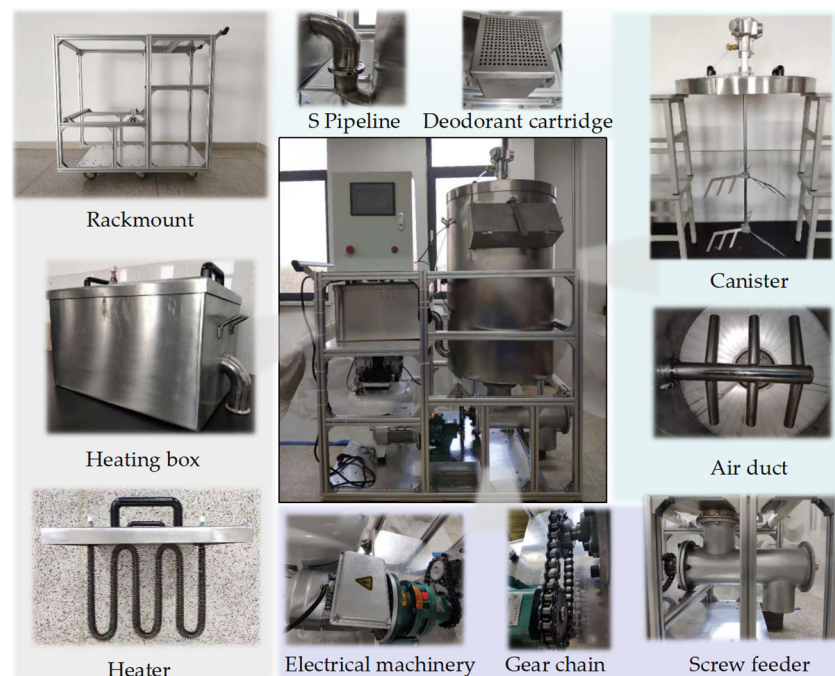


Figure 12. Installation chart of each component of composting equipment.

2.3. Design and Installation of Composting Control System

2.3.1. System Design

The temperature and oxygen content of the compost within the tank are the main factors used by the composting control system to operate motors, electric heaters, and air pumps. The device automatically modifies the air pumps' and heaters' operation by keeping an eye on these parameters. The heater is used to keep the compost at a temperature between 55 °C and 65 °C [50,51]. It turns on when the temperature falls below 55 °C and turns off when it rises beyond 65 °C. When the oxygen concentration drops below 15%, the air pump should be used to introduce room-temperature air, maintaining the concentration between 15% and 20%. With a touch screen that has a primary interface, control interface, and display interface, the system can be operated in both automated and manual modes.

A detection unit and a control unit make up the compost control system. In addition to sensors for air temperature, humidity, and oxygen concentration, the detecting unit also has sensors for soil temperature and humidity. The PLC, intermediate relays, and touch screen make up the control unit. Human-machine interaction is facilitated by the

Kunlun TPC7062Ti touch screen, which uses MCGS2018 embedded software to allow for process animation display, real-time data storage, and historical data export. The PLC is configured to control the temperature and oxygen content of the compost by connecting to the touch screen via the RS485 interface. In reaction to variations in sensor data, it initiates and stops the air pump and heater automatically, ensuring that the fermentation process runs smoothly.

2.3.2. System Installation and Commissioning

After the PLC pre-programming and touch screen interface configuration design are finished, the compost control system may be installed and put into service. On the central sidewall of the fermenter, sensors for measuring soil temperature and humidity are installed to track the compost's temperature and humidity in real time. To monitor the properties of the air, sensors for oxygen content, humidity, and air temperature are fixed on the top side wall of the fermenter. The placements of the sensors are shown in Figure 13.



Figure 13. Installation position of each sensor. (a) Installation location of soil temperature–humidity sensor; (b) installation location of air temperature–humidity–oxygen concentration sensor.

The actual assembly of the control box is shown in Figure 14.



Figure 14. Control box of composting equipment.

3. Experimental Verification of the Practicality of Composting Equipment

After the installation and commissioning of the equipment, the system was employed in actual composting experiments to verify its feasibility and efficiency. Manual control was implemented to regulate fermentation conditions during the experiments, as the automatic mode is designed for external heating rather than natural fermentation. The primary objective of the equipment is to enhance the decomposition of organic matter through external heating and improve fertilizer maturity. In this study, experimental analyses were conducted to compare the two composting technologies and to evaluate the equipment's role in improving the quality of organic fertilizers.

3.1. Pre-Preparation for Composting Trials

3.1.1. Compost Feedstock

Corn stover and sheep dung were used as composting ingredients in this investigation. China's Inner Mongolia Autonomous Region has a plentiful supply of sheep dung, which causes serious problems with manure buildup. Furthermore, Inner Mongolia is one of China's main regions for maize farming, yielding a lot of straw that is rich in organic matter after harvest. By adding more organic matter to the compost material, this straw may raise the value of the finished product. In Salazhi Town, Tumet Right Banner, Baotou City, Inner Mongolia, there is a fertilizer manufacturing factory where the sheep manure used for the composting test was obtained. The maize stover was acquired from Inner Mongolia Agricultural University's Agricultural Machinery Laboratory. Crushed straw made up both materials, as Figure 15 illustrates.



Figure 15. Composting materials.

3.1.2. Other Test Materials and Instruments

In addition to the composting materials, various supplies, equipment, and materials were selected for this trial. These included fermenters, activated charcoal, mung bean seeds, agricultural soil, Petri dishes, glass measuring cylinders, and sprayers. Figure 16 illustrates the specific items used in the experiment.



Figure 16. Other test materials and instruments.

3.1.3. Pre-Test

The hot-air unit used in this study heats air through an electric heating element. After preheating, an air pump is activated to supply hot air to the compost, which must reach a temperature above 80 °C. To determine the appropriate preheating time, a preliminary test can be conducted prior to the composting experiment. A miniature temperature sensor

monitors the air temperature at the outlet of the heated box, and the data indicate that the air temperature rises from room temperature to above 80 °C in approximately 31 s. Before the experiment, the carbon-to-nitrogen (C/N) ratio of the mixed compost was measured to ensure that it was within an appropriate range. A suitable C/N ratio is essential to reach thermophilic temperatures under natural aeration conditions.

3.1.4. Test Methods

During the composting process, the initial mass ratio of sheep excreta to corn stover was set at 20:1, and the initial water content was adjusted to a desired ratio of 1:2. The composting material was introduced into the fermenter through the equipment, with water and composting materials gradually added. The feeding process occurred in six stages, with each stage carefully weighed and recorded. No electric heater was used during the experiment; instead, the material was warmed through natural fermentation and periodically rotated. Data collection included measurements of ambient temperature, oxygen concentration in the tank, air temperature, humidity, and compost temperature. For analysis, records were taken at 9:00, 15:00, and 21:00 daily.

Fresh compost samples were kept fresh at 4 °C in order to calculate the germination index. In order to aid in the extraction of organic components, the samples were first carefully mixed with ultrapure water at a ratio of 1:10 (w/v) and put in a horizontal shaker for two hours. The mixture was then sent to a centrifuge, where the solid particles were separated for 10 min at a predefined speed. To get rid of any leftover suspension, filter paper was used to filter the supernatant after centrifugation. Using a pipette, we precisely measured five millilitres of filtrate and transferred it to sterile Petri dishes that had been prepared with filter paper beforehand. To guarantee uniformity throughout the experiment, 20 morphologically uniform and healthy cabbage seeds were placed in each Petri dish. For the duration of the germination trials, the Petri dishes were kept at a steady temperature and protected from light for four to seven days. In order to evaluate the impact of the compost extract on seed germination, ultrapure water was used as the control. For every sample, a minimum of four biological duplicates were conducted. In Figure 17, the precise process is shown.

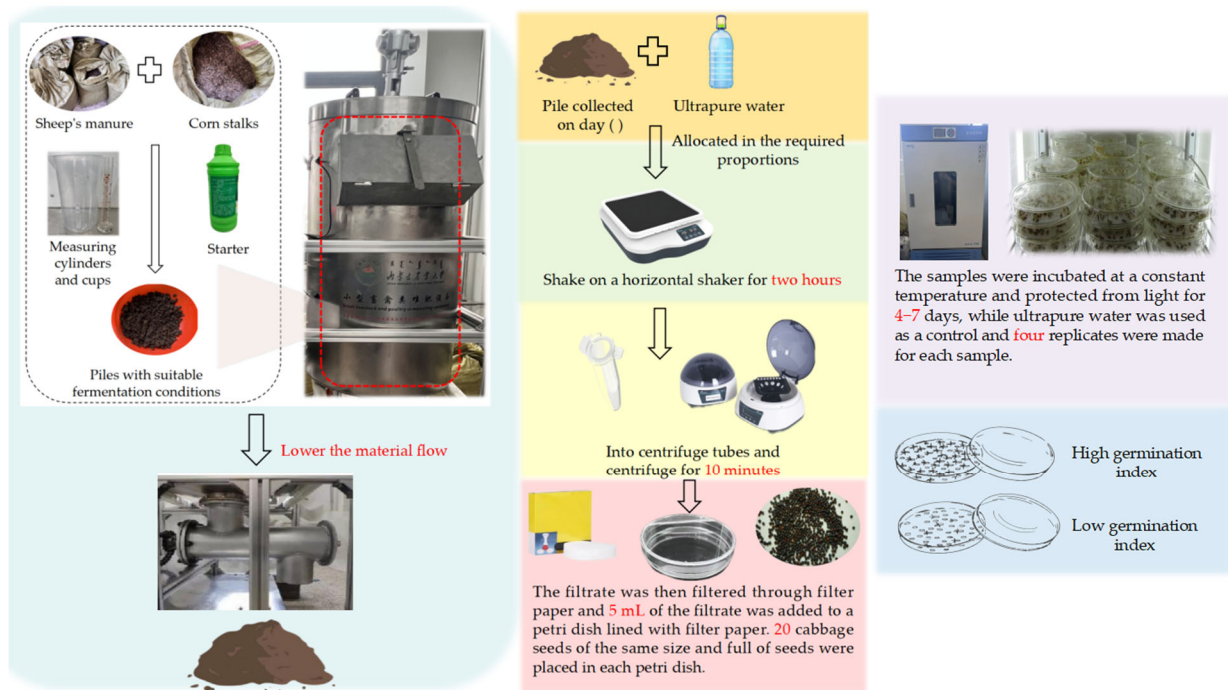


Figure 17. Test method flow chart.

3.2. Comparison of Composting Effects Under Different Conditions

3.2.1. The Change in Composting Materials' Temperature

The temperature of compost is a key factor in determining its quality. A proper temperature range must be maintained to ensure the safety and quality of the compost product. Figure 18 shows the temperature variations in the composting of sheep manure.

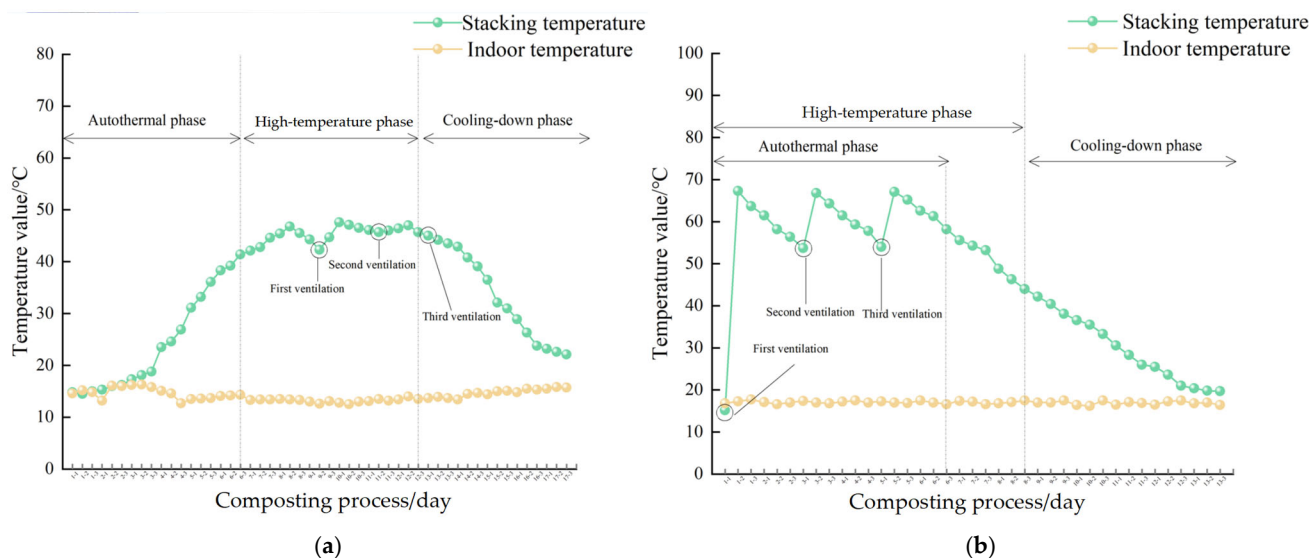


Figure 18. The change in composting materials' temperature. (a) Composting trials under natural warming conditions; (b) composting trials under artificially warmed conditions.

Under natural warming circumstances, the compost pile reached the high-temperature stage after about 6 days, as Figure 18a illustrates. On day nine, when the pile temperature started to drop, the first aeration mixing took place. After this, there was a little rise in the pile temperature, peaking at 47.6 °C. Because the pile temperature was dropping, two further aeration mixings were carried out over the course of the next four days. The temperature rose after the second aeration, although it did not go over the previous high. The temperature steadily dropped to just over room temperature after the third aeration, indicating that the breakdown process was finished. In this test, the composting process took 17 days, divided into three phases: a warming phase that lasted about 6 days, a high-temperature phase that lasted around 6 days, and a cooling phase that lasted roughly 5 days.

In order to progress the compost to the high-temperature stage and raise the temperature during this phase, which helps to speed up the fermentation process, the hot-air unit was turned on in this composting experiment. The hot-air device was switched on for aeration and heating after all of the compost had been poured into the fermenter. The device was then turned off when the compost temperature had risen over 65 °C. The hot-air device was restarted if, during the following composting process, the temperature of the compost fell below 55 °C. The significant differences between this experiment and the previous one were the temperature of the high-temperature phase and the existence of a warming phase, as well as the frequency and length of pile aeration and stirring.

This composting study lasted 13 days in total, as Figure 18b illustrates. About six days passed during the high-temperature period with artificial aeration and heating. After around two days into the next cooling phase, the compost temperature dropped to a low of 40 °C. This time frame may still be regarded as a component of the high-temperature phase of compost fermentation, however, in contrast to the natural fermentation experiment. With artificial warming, the high-temperature period lasted around 8 days, during which the pile's highest temperature was 67.3 °C. The fermenter was held for about 42 h, as shown by the roughly 42 h gap between the subsequent heating and aeration processes.

3.2.2. The Change in Composting Materials' Humidity

To keep the microbial life in the compost active, proper humidity levels must be maintained. The nutritional value and acceptability of the compost product are ultimately determined by the breakdown and transformation of organic waste, which is carried out by these microorganisms. The fluctuation in humidity throughout the composting process is seen in Figure 19.

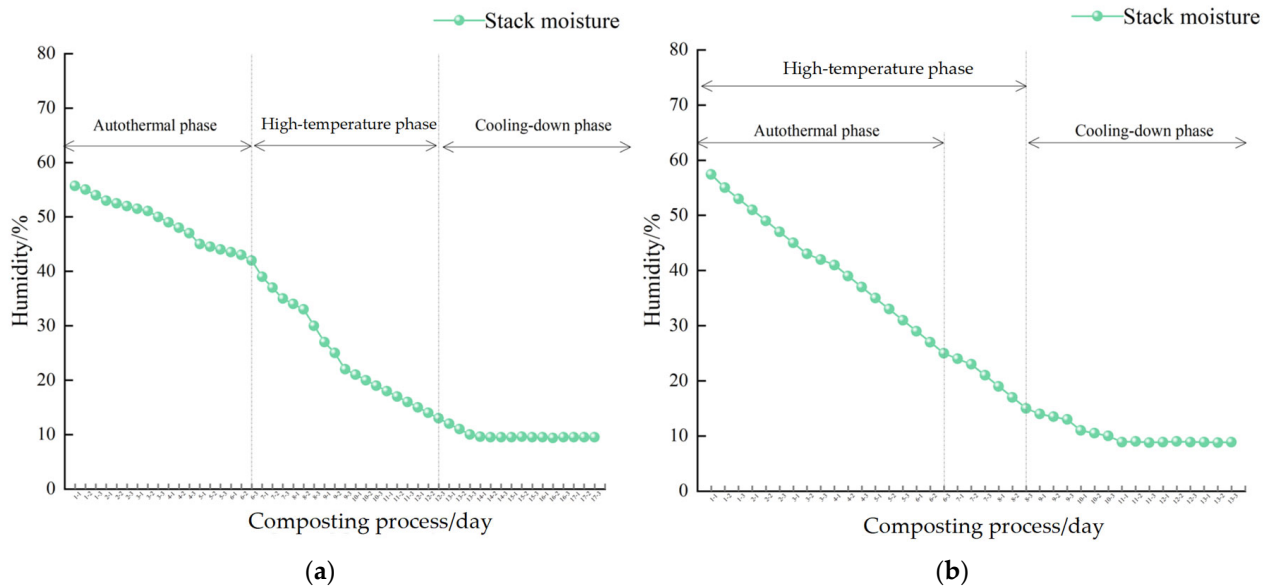


Figure 19. The change of composting materials' humidity. (a) Composting trials under natural warming conditions; (b) composting trials under artificially warmed conditions.

The relationship between the rise in pile temperature and the change in pile humidity is seen in Figure 19a. As the pile temperature increases, the general pattern shows that the humidity is continuously decreasing. When compared to the heating-up and cooling-down stages, the fall in pile humidity during the high-temperature period occurs much quicker, eventually stabilizing at around 10%. In a similar vein, Figure 19b illustrates how the moisture content of the pile steadily drops as composting advances. When the temperature is high, the rate of reduction is faster; however, as the temperature drops, this slows down and eventually stabilizes at around 9%.

3.2.3. The Change in Oxygen Concentration in the Tank

Aerobic bacteria thrive in an ideal metabolic environment when there is an appropriate concentration of oxygen, which is usually advised to be between 15% and 20%. This helps preserve the quality of compost by accelerating the breakdown of organic waste. The variations in oxygen content throughout the composting process are seen in Figure 20.

The oxygen content in the fermenter progressively drops as the organic matter breaks down, as shown in Figure 20a. But after every aeration and stirring, it rises once again, keeping the concentration over 15% overall. Similar to Figure 20b, the oxygen content in the tank falls as a result of compost fermentation but increases after each aeration. Since the compost is largely broken down during the chilling phase, less oxygen is used. The oxygen content in the tank somewhat rises in the last stages of composting because the fermenter is semi-closed.

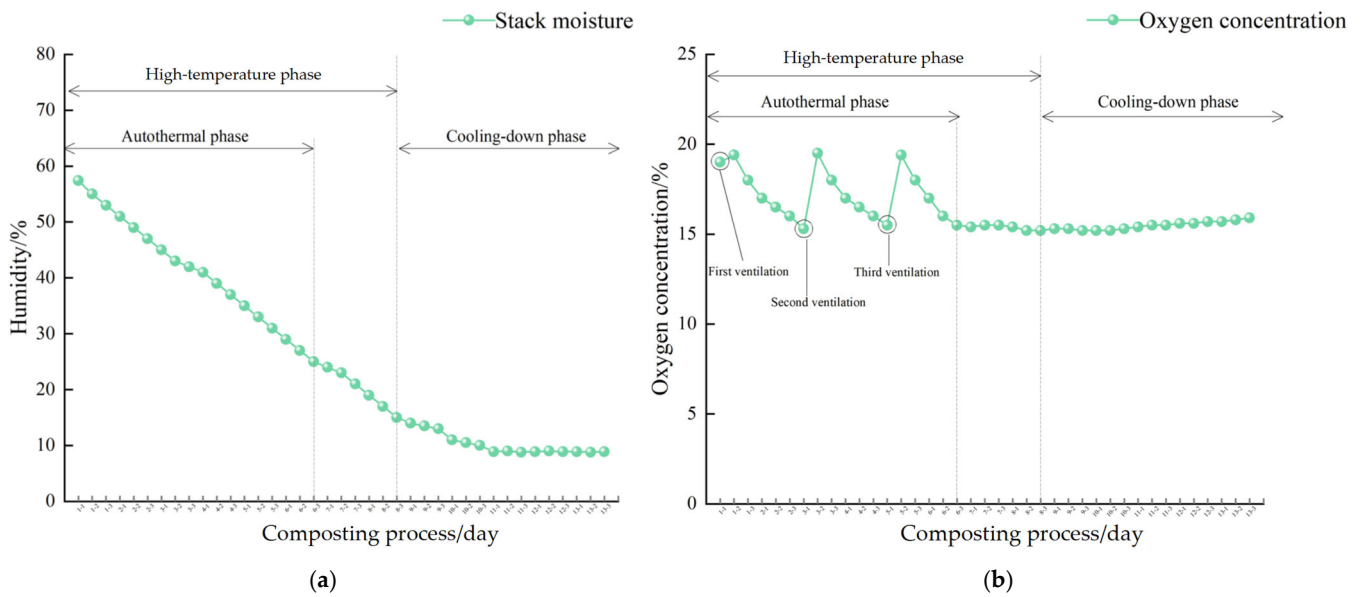


Figure 20. The change in oxygen concentration in the tank. (a) Composting trials under natural warming conditions; (b) composting trials under artificially warmed conditions.

3.2.4. The Change in pH During Composting

The present investigation used the seed germination index (GI) and pH value as indicators to assess compost maturity. After the natural compost pile reached the high-temperature stage on the seventh day, the average GI was computed and the pH value of the samples was measured and recorded. Furthermore, samples were collected to determine the pH and GI after the conclusion of the artificial warming phase, beginning on the seventh day. The quality of the finished compost depends heavily on the acid–base balance, or pH, of the composting process. The dynamic trends of pH throughout the composting process are shown in Figure 21.

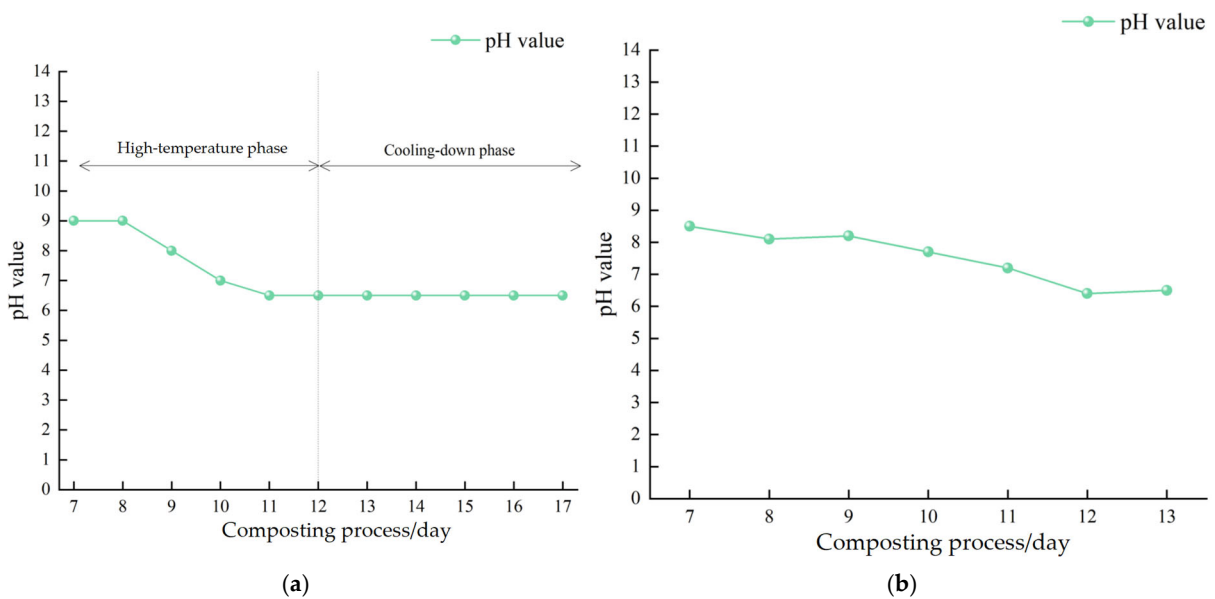


Figure 21. Test results for pH. (a) Composting trials under natural warming conditions; (b) composting trials under artificially warmed conditions.

The pH of the compost changes from weakly alkaline to weakly acidic throughout the middle and late phases of composting, as shown in Figure 21a. The organic matter’s

breakdown products are thought to be responsible for this alteration. In line with the findings of the natural fermentation composting test, Figure 21b also depicts a similar pH shift throughout the middle and late phases of composting.

3.2.5. The Change in GI During Composting

The seed germination index (GI), which may be used to gauge the phytotoxicity of reactor samples, is a crucial measurement of the amount of compounds in compost that restrict plant development. Figure 22 shows the GI changes that occur throughout the composting process.

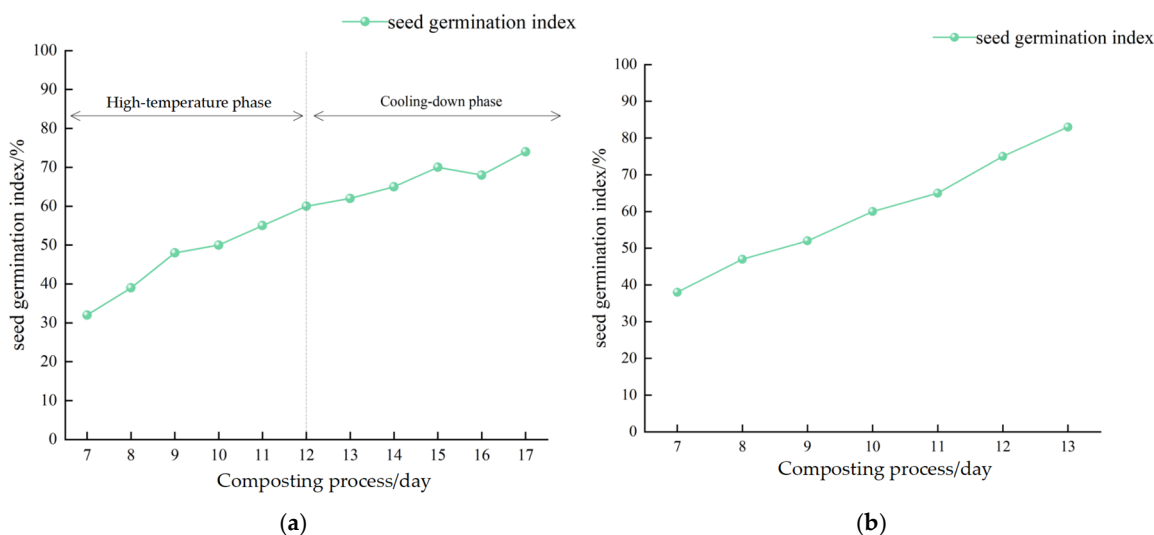


Figure 22. Test results for GI. (a) Composting trials under natural warming conditions; (b) composting trials under artificially warmed conditions.

According to Figure 22a, when fermentation occurs naturally, the compost's seed germination index (GI) approaches 74%. Similarly, Figure 22b demonstrates that the compost pile's GI reaches around 83% during decomposition in hot, artificially aerated circumstances.

3.3. Comparison of Test Results and Evaluation of Equipment Practicality

The compost spoils faster and reaches a higher temperature during the high-temperature stage when heated artificially. In contrast, compost fermentation takes longer to reach the high-temperature stage when exposed to natural warming circumstances. This is because temperature rises more slowly and becomes less efficient, resulting in a lengthier high-temperature period. The pre-compost warming step of natural fermentation composting takes a long time, which adds to the total duration of the composting process. With the help of a hot gas appliance, composting that has been artificially heated skips the lengthy warming stage and goes straight into the high-temperature phase, which raises the temperature at which compost ferments and drastically reduces the amount of time it takes to compost. As per the Technical Specification for Harmless Treatment of Livestock and Poultry Manure (GB/T 36195-2018), which is a national standard, the compost pile's temperature must be kept above 50 °C for a minimum of 7 days or above 45 °C for a minimum of 14 days [50]. The pile's greatest temperature under naturally occurring warming circumstances was below 50 °C, and it only stayed between 45 °C and 50 °C for three to four days, falling short of the required national temperature. In contrast, the pile's temperature met the national threshold for around 7–8 days under artificial warming circumstances.

Under both composting techniques, the trends in the pile's humidity and oxygen content were comparable. Under the artificial heating process, however, the humidity dropped more quickly. As the pile fermented and the air pump aerated, the concentration of oxygen changed. When it came to decomposition, the seed germination index (GI) improved during the course of the composting process and reached a greater level when

heated artificially. This suggests that the compost decomposed more fully and that the organic matter broke down more thoroughly. In the middle and late phases of composting, the compost shifted from being weakly alkaline to weakly acidic using both techniques, demonstrating how the breakdown products of organic matter have a significant impact on the pH value of the fertilizer.

According to the industry standard “Organic Fertilizer” (NY/T 525-2021), decomposed organic fertilizer must have a pH of between 5.5 and 8.5 and less than 30% water content [51]. The test findings demonstrate that the pH and water content criteria are met by the organic fertilizer generated under both circumstances. In order to assess fertilizer breakdown, the compost test used the GI as a measure. A GI greater than 70% indicates that the compost is fully digested and essentially not phytotoxic. Under natural warming conditions, the GI of the resulting compost is approximately 74%, while under artificial warming, it rises to 83%. This higher GI under artificial warming is more in line with the low phytotoxicity criterion for organic fertilizers.

The composting equipment created in this research can effectively boost the temperature of compost fermentation and shorten the composting cycle, enhancing the efficiency of compost maturation, as shown by the analysis and comparison of the two composting tests. This solves the conventional composting problems of poor efficiency, heat dispersion, and difficulties in increasing temperature. With a more complete breakdown of organic waste, the organic fertilizer generated by this equipment is more mature than that produced by spontaneous fermentation, causing less damage to crops. This composting apparatus has a feeding device, air pump, electric heater, and stirrer. It successfully raises the utilization value of the resultant organic fertilizer and increases the composting efficiency of animal and poultry manure via the synergistic operation of these components and the real-time control of the composting system. Thus, real composting experiments have proven the design feasibility and practical performance of this composting equipment.

4. Discussions

This research examined how artificial heating and natural warming affect compost spoilage time, temperature management, and overall composting efficiency. The results show that artificial heating significantly reduces spoilage time and raises temperatures during the high-temperature phase. This is achieved by bypassing the prolonged warming typically observed in spontaneous fermentation. Elevated temperatures are essential for efficient composting, as defined by the Technical Specification for Harmless Treatment of Livestock and Poultry Manure (GB/T 36195-2018). Artificial heating consistently maintains temperatures over 50 °C for 7–8 days, unlike natural warming, which cannot sustain such conditions.

Although both composting methods showed similar trends in humidity and oxygen levels, artificial heating accelerates moisture loss, which could hinder microbial activity if moisture becomes too low. It is crucial to balance moisture levels to facilitate microbial processes. Furthermore, while artificial heating improves the seed germination index (GI), indicating a more complete decomposition of organic matter, maintaining adequate moisture is essential for optimal microbial function.

When comparing these results with other studies, it is evident that temperature control is pivotal for achieving consistent compost quality. The observed improvement in GI is consistent with recent findings highlighting enhanced organic material breakdown. Additionally, the pH shift from weakly alkaline to weakly acidic underscores significant organic matter decomposition. The standards cited in this study (NY/T 525-2021) focus on pH, moisture content, and pathogen reduction, but should be expanded to include parameters like electrical conductivity, which are critical for a comprehensive assessment of compost quality.

Both composting methods met the standard pH requirement of 5.5 to 8.5 and maintained moisture content below 30%. However, only the artificially heated compost reached a GI value over 80%, signifying complete decomposition and low phytotoxicity. This high-

lights the need for updated standards that incorporate a wider range of compost quality indicators beyond pH and GI.

The findings emphasize the effectiveness of the newly developed composting apparatus in overcoming traditional challenges like temperature control and heat retention. This equipment minimizes crop damage by producing a more mature organic fertilizer through thorough organic matter decomposition. Enhanced efficiency is achieved through the integration of an air pump, electric heater, stirrer, feeding device, and real-time control features. The equipment's effectiveness and practical performance were validated through actual composting tests, demonstrating its potential to advance conventional composting techniques while adhering to comprehensive quality standards.

5. Conclusions

(1) Comparison of Composting Conditions: This study comprehensively compared the effects of artificially heated and naturally warmed composting conditions on spoilage time, temperature regulation, and overall composting efficiency. The findings demonstrate that artificially heated composting significantly shortens the composting cycle by directly entering the high-temperature phase, bypassing the prolonged warming stage characteristic of natural fermentation. This method achieves higher and more sustained temperatures during the high-temperature stage, effectively meeting the national standard (GB/T 36195-2018) requirements for safe and effective composting.

(2) Humidity and Oxygen Trends: This study revealed that both composting methods exhibited similar trends in humidity and oxygen concentration, with a faster decrease in humidity observed under artificial heating. The seed germination index (GI), an indicator of compost decomposition and phytotoxicity, was significantly higher under artificial heating, suggesting a more complete breakdown of organic matter. Both composting methods resulted in a shift from weakly alkaline to weakly acidic pH values, influenced by the decomposition products of organic matter.

(3) Quality of Organic Fertilizers: The organic fertilizers produced under both conditions met the industry standard (NY/T 525-2021) for water content and pH. However, only the artificially heated compost reached a GI value of 80% or more, indicating that it was fully decomposed and not phytotoxic. In contrast, naturally heated compost did not achieve the same level of effectiveness as that produced using composting equipment.

(4) Validation of Composting Equipment: This study validates the efficacy of the designed composting equipment, which integrates an air pump, electric heater, stirrer, and feeding device. This equipment addresses traditional composting challenges, such as difficulty in raising temperature, heat dissipation, and low efficiency. The resulting organic fertilizer from this equipment is more mature and has a more thorough organic matter decomposition, reducing potential harm to crops. These findings confirm the practical effectiveness and feasibility of the composting equipment, highlighting its potential to significantly improve traditional composting methods for livestock and poultry manure.

Author Contributions: Conceptualization, methodology, writing—original draft preparation, investigation, writing—review and editing, and supervision, J.W.; validation, formal analysis, and writing—review and editing, K.R. and L.Z. All authors have read and agreed to the published version of the manuscript.

Funding: This work was supported by the Innovation Team of Higher Education Institutions in Inner Mongolia Autonomous Region, grant number NMGIRT2312; Modern Agriculture and Inner Mongolia Grassland Talent Innovation Team, grant number No. [2018] 19; Inner Mongolia Autonomous Region “First-Class Discipline Research Special Project” (Grassland and Special Economic Crop and Food Industry Chain Intelligent Equipment Creation, project number: YLXKZX-NND-046); and Inner Mongolia Autonomous Region “First-Class Discipline Research Special Project” (Research and Development of Inner Mongolia’s Characteristic Economic Minor Grain Crop Systems and Intelligent Equipment, project number: YLXKZX-NND-050).

Institutional Review Board Statement: Not applicable.

Informed Consent Statement: Not applicable.

Data Availability Statement: Data are contained within the article.

Acknowledgments: The authors sincerely thank the anonymous reviewers for their critical comments and suggestions for improving the manuscript.

Conflicts of Interest: The authors declare no conflicts of interest.

Abbreviations

MCGS	Monitor and control generated system
PLC	Programmable logic controller
°C	Anders Celsius
kJ	Kilojoules
h	Hour
K	Kelvins
m ³	Cubic meter
mm	Millimetre
W	Watt
GI	Germination index
PH	Potential of hydrogen
q_{eht}	Heat released by the electric heating tube
q_{hc}	The heat absorbed by the air pump during heating
q_{ste}	Heat conduction on the wall of the heating box
q_{ste}	Heat absorbed by water evaporation in the air
q_{else}	Other forms of heat loss
c_{air}	Specific heat capacity of air
ρ_{air}	Air density
ϕ_{air}	Ventilation capacity
ΔT_{air}	Air temperature change value
λ_{air}	Air thermal conductivity
A	Contact area
ΔT	Temperature difference between objects
d	Heat transfer distance
Δx	Net mass of water vapor in the air
q_l	Enthalpy value of water vapor

References

- Chen, Y.; Yu, F.; Liang, S. Utilization of solar energy in sewage sludge composting: Fertilizer effect and application. *Waste Manag.* **2014**, *34*, 2014–2021. [[CrossRef](#)]
- Jeong, K.H.; Kim, J.K.; Khan, M.A. A Study on the Characteristics of Livestock Manure Treatment Facility in Korea. *Arkhiv. Patol.* **2014**, *22*, 28–44.
- Kasinski, S.; Slota, M.; Markowski, M. Municipal waste stabilization in a reactor with an integrated active and passive aeration system. *Waste Manag.* **2016**, *50*, 31–38. [[CrossRef](#)]
- Shimizu, N.; Karyadi, J.N.W.; Harano, M. Cattle manure composting in a packed-bed reactor with forced aeration strategy. *Eng. Agric. Environ. Food* **2018**, *11*, 65–73. [[CrossRef](#)]
- Taeporamaysamai, O.; Ratanatamskul, C. Co-composting of various organic substrates from municipal solid waste using an on-site prototype vermicomposting reactor. *Int. Biodeterior. Biodegrad.* **2016**, *113*, 357–366. [[CrossRef](#)]
- Chen, W.; Luo, S.; Du, S. Strategy to Strengthen Rural Domestic Waste Composting at Low Temperature: Choice of Ventilation Condition. *Waste Biomass Valorization* **2020**, *11*, 6649–6665. [[CrossRef](#)]
- Puspitaloka, H.; Mimoto, H.; Tran, Q.N.M.; Koyama, M.; Nakasaki, K. Effect of aeration method on organic matter degradation and ammonia emission of composting in a laboratory-scale reactor. *J. Mater. Cycles Waste Manag.* **2020**, *22*, 604–609. [[CrossRef](#)]
- Sen, Y.; Min, T.; Yaru, C.; Tipeng, W.; Changming, S. Study on mixed compost of cattle dung and corn stalk biogas residue and its impact on environment. *J. Chin. Agric. Mech.* **2023**, *44*, 168–173.
- Zhou, H.; Di, L.; Hua, X.; Deng, T. The Addition of a Small Dose of Cinnamomum camphora Biomass Unexpectedly Enhanced Lignocellulose Degradation during the Compost of Stropharia rugosoannulata Cultivation Materials. *Sustainability* **2023**, *15*, 10483. [[CrossRef](#)]
- Wu, Y.; Luo, Z.; Qi, L.; Zhang, R.; Wang, Y. A Study of the Relationship between Initial Grape Yield and Soil Properties Based on Organic Fertilization. *Agronomy* **2024**, *14*, 861. [[CrossRef](#)]

11. Li, Y.; Li, Q.; Ji, Z.; Andom, O.; Wang, X.; Guo, X.; Li, Z. Current Status and Spatiotemporal Evolution of Antibiotic Residues in Livestock and Poultry Manure in China. *Agriculture* **2023**, *13*, 1877. [\[CrossRef\]](#)
12. Zhang, X.A. Research on Nitrogen Loss and In-Situ Nitrogen Conservation in High Temperature Composting of Manure. Master's Thesis, Chongqing Technology and Business University, Chongqing, China, 2018.
13. Jiang, Y.; Zhang, Q.; Niu, J.; Wu, J. Pastoral Population Growth and Land Use Policy Has Significantly Impacted Livestock Structure in Inner Mongolia—A Case Study in the Xilinhot Region. *Sustainability* **2019**, *11*, 7208. [\[CrossRef\]](#)
14. Aricha, H.; Simujide, H.; Wang, C.; Zhang, J.; Lv, W.; Jimisi, X.; Liu, B.; Chen, H.; Zhang, C.; He, L.; et al. Comparative Analysis of Fecal Microbiota of Grazing Mongolian Cattle from Different Regions in Inner Mongolia, China. *Animals* **2021**, *11*, 1938. [\[CrossRef\]](#)
15. Liu, Y.; Wang, P.; Wang, R.; Li, J.; Zhai, B.; Luo, X.; Yang, X. An Epidemiological Investigation and Drug-Resistant Strain Isolation of *Nematodirus oiratianus* in Sheep in Inner Mongolia, China. *Animals* **2023**, *13*, 30. [\[CrossRef\]](#)
16. Wang, F. Design and Experiment of Small Composting Equipment for Fecal Matter of Livestock and Poultry Based on Heating by Aeration. Master's Thesis, Inner Mongolia Agricultural University, Hohhot, China, 2021.
17. Li, L.-T.; Li, W.-M.; Sun, J.-M.; Chu, F.; Rao, Z.X.; Huang, F.-Q. Research status and prospects of the resource utilization of organic waste in urban and rural areas. *J. Agric. Resour. Environ.* **2019**, *36*, 264–271.
18. Zhao, C.; Wu, B.; Hao, W. Dynamic Changes in Physicochemical Properties and Microbial Community in Three Types of Recycled Manure Solids for Dairy Heifers. *Agronomy* **2024**, *14*, 1132. [\[CrossRef\]](#)
19. Zając, M.; Skrajna, T. Effect of Composted Organic Waste on *Miscanthus sinensis* Andersson Energy Value. *Energies* **2024**, *17*, 2532. [\[CrossRef\]](#)
20. Zhen, X.; Tan, C.; Li, Z. Humus Transformation and Compost Maturity Indexes in High-Temperature Composting of Livestock and Poultry Manure. *J. Biobased Mater. Bioenergy* **2022**, *16*, 329–335. [\[CrossRef\]](#)
21. Lu, W.; Gao, Y.; Jian, L. Application effect of sheep manure on plant and soil. *Acta Ecol. Anim. Domastici* **2019**, *40*, 86–90.
22. González, R.; Blanco, D.; Cascallana, J.G.; Carrillo-Peña, D.; Gómez, X. Anaerobic Co-Digestion of Sheep Manure and Waste from a Potato Processing Factory: Techno-Economic Analysis. *Fermentation* **2021**, *7*, 235. [\[CrossRef\]](#)
23. Al-Suhaibani, N.; Selim, M.; Alderfasi, A.; El-Hendawy, S. Integrated Application of Composted Agricultural Wastes, Chemical Fertilizers and Biofertilizers as an Avenue to Promote Growth, Yield and Quality of Maize in an Arid Agro-Ecosystem. *Sustainability* **2021**, *13*, 7439. [\[CrossRef\]](#)
24. Kureljušić, J.M.; Vesković Moračanin, S.M.; Đukić, D.A.; Mandić, L.; Đurović, V.; Kureljušić, B.I.; Stojanova, M.T. Comparative Study of Vermicomposting: Apple Pomace Alone and in Combination with Wheat Straw and Manure. *Agronomy* **2024**, *14*, 1189. [\[CrossRef\]](#)
25. Cai, S.; Ma, Y.; Bao, Z.; Yang, Z.; Niu, X.; Meng, Q.; Qin, D.; Wang, Y.; Wan, J.; Guo, X. The Impacts of the C/N Ratio on Hydrogen Sulfide Emission and Microbial Community Characteristics during Chicken Manure Composting with Wheat Straw. *Agriculture* **2024**, *14*, 948. [\[CrossRef\]](#)
26. Rodrigues, T.F.; Itkes, M.P.M.; Brogiato, G.; Marques, V.A.R.; Martins, V.; Villarraga, C.O.; Esposito, E. Agroecological Transformation: Implementation of an Agroforestry System in a Construction Debris Area Focusing on Vegetables Development through Microbial Treatments. *Appl. Sci.* **2024**, *14*, 4648. [\[CrossRef\]](#)
27. Netthisinghe, A.; Woosley, P.; Strunk, W.; Agga, G.; Sistani, K. Composting Dairy Manure with Biochar: Compost Characteristics, Aminopyridine Residual Concentrations, and Phytotoxicity Effects. *Agronomy* **2024**, *14*, 952. [\[CrossRef\]](#)
28. Chen, L.; Zhang, H.; Jia, X.; Fang, Y.; Lin, C. Soil Fertility and Bacterial Community Composition in Response to the Composting of Biochar-Amended Chicken Manure. *Agronomy* **2024**, *14*, 886. [\[CrossRef\]](#)
29. Wang, J.; Zhang, B.; Wang, J.; Zhang, G.; Yue, Z.; Hu, L.; Yu, J.; Liu, Z. Effects of Different Agricultural Waste Composts on Cabbage Yield and Rhizosphere Environment. *Agronomy* **2024**, *14*, 413. [\[CrossRef\]](#)
30. Alkarimiah, R.; Suja, F. Composting of EFB and POME Using a Step-Feeding Strategy in a Rotary Drum Reactor: The Effect of Active Aeration and Mixing Ratio on Composting Performance. *Ecol. Environ. Conserv.* **2020**, *26*, 2543–2553. [\[CrossRef\]](#)
31. Zhou, X.; Yang, J.; Xu, S. Rapid in-situ composting of household food waste. *Process Saf. Environ. Prot.* **2020**, *20*, 259–266. [\[CrossRef\]](#)
32. Yuriandala, Y.; Laily, N.; Maziya, F.B. Vegetable Waste and Food Waste Treatment Using Modified Aerobic Composting Reactor. *Appl. Mech. Mater.* **2020**, *4392*, 16–22. [\[CrossRef\]](#)
33. Awasthi, M.K.; Singh, E.; Binod, P.; Sindhu, R.; Sarsaiya, S.; Kumar, A.; Chen, H.; Duan, Y.; Pandey, A.; Kumar, S.; et al. Biotechnological strategies for bio-transforming biosolid into resources toward circular bio-economy: A review. *Renew. Sustain. Energy Rev.* **2022**, *156*, 111987. [\[CrossRef\]](#)
34. Romano, E.; Brambilla, M.; Bisaglia, C.; Assirelli, A. Using Image Texture Analysis to Evaluate Soil–Compost Mechanical Mixing in Organic Farms. *Agriculture* **2023**, *13*, 1113. [\[CrossRef\]](#)
35. Li, D.; Qi, C.; Wei, Y.; Li, G. Measurement of pollution production coefficient of sheep breeding industry in Northern China. *Trans. Chin. Soc. Agric. Eng.* **2021**, *37*, 220–227.
36. Gottschall, R.; Thelen-Jüngling, M.; Kranert, M.; Kehres, B. Suitability of Biowaste and Green Waste Composts for Organic Farming in Germany and the Resulting Utilization Potentials. *Agriculture* **2023**, *13*, 740. [\[CrossRef\]](#)

37. Wang, Q.; Awasthi, M.K.; Zhao, J.; Ren, X.; Li, R.; Wang, Z.; Wang, M.; Zhang, Z. Improvement of pig manure compost lignocellulose degradation, organic matter humification and compost quality with medical stone. *Bioresour. Technol.* **2017**, *243*, 771–777. [[CrossRef](#)]
38. Agegnehu, G.; Bass, A.M.; Nelson, P.N.; Muirhead, B.; Wright, G.; Bird, M.I. Biochar and biochar-compost as soil amendments: Effects on peanut yield, soil properties and greenhouse gas emissions in tropical North Queensland, Australia. *Agric. Ecosyst. Environ.* **2015**, *213*, 72–85. [[CrossRef](#)]
39. Awasthi, M.K.; Pandey, A.K.; Bundela, P.S.; Wong, J.W.C.; Li, R.; Zhang, Z. Co-composting of gelatin industry sludge combined with organic fraction of municipal solid waste and poultry waste employing zeolite mixed with enriched nitrifying bacterial consortium. *Bioresour. Technol.* **2016**, *213*, 181–189. [[CrossRef](#)]
40. Huo, L.; Zhao, L.; Meng, H.; Yao, Z. Study on straw multi-use potential in China. *Trans. Chin. Soc. Agric. Eng.* **2019**, *35*, 218–224.
41. Sobieraj, K.; Stegenta-Dąbrowska, S.; Zafiu, C.; Binner, E.; Białowiec, A. Carbon Monoxide Production during Bio-Waste Composting under Different Temperature and Aeration Regimes. *Materials* **2023**, *16*, 4551. [[CrossRef](#)]
42. Sobieraj, K.; Stegenta-Dąbrowska, S.; Luo, G.; Koziel, J.A.; Białowiec, A. Biological treatment of biowaste as an innovative source of CO—The role of composting process. *Front. Bioeng. Biotechnol.* **2023**, *11*, 1126737.
43. Stegenta-Dąbrowska, S.; Drabczyński, G.; Sobieraj, K.; Koziel, J.A.; Białowiec, A. The Biotic and Abiotic Carbon Monoxide Formation during Aerobic Co-digestion of Dairy Cattle Manure with Green Waste and Sawdust. *Front. Bioeng. Biotechnol.* **2019**, *7*, 283. [[CrossRef](#)] [[PubMed](#)]
44. Lu, Y.; Chadwick, D.; Norse, D.; Powlson, D.; Shi, W. Sustainable intensification of China’s agriculture: The key role of nutrient management and climate change mitigation and adaptation. *Agric. Ecosyst. Environ.* **2015**, *209*, 1–4. [[CrossRef](#)]
45. Gilbert, J.; Siebert, S. *ECN Data Report 2022. Compost and Digestate for a Circular Bioeconomy. Overview of Bio-Waste Collection, Treatment & Markets Across Europe*; European Compost Network ECN e.V: Bochum, Germany, 2022.
46. Shrestha, P.P.; Ghimire, A.; Dangi, M.B.; Urynowicz, M.A. Development of a Municipal Solid Waste Management Life Cycle Assessment Tool for Banepa Municipality, Nepal. *Sustainability* **2023**, *15*, 9954. [[CrossRef](#)]
47. Prommuak, C.; Jarunglumert, T.; Putmai, N. Comparative study on different turning device alignments for household food waste composters. *Environ. Prog. Sustain. Energy* **2018**, *37*, 1954–1958. [[CrossRef](#)]
48. Schneider, J.; Burg, J.M.; Theilen, U. Towards optimized drum composting: Evaluation of the radial mixing performance of a model substrate on the laboratory scale. *Environ. Technol.* **2020**, *41*, 1606–1613. [[CrossRef](#)]
49. Wang, Y.; Pang, L.; Liu, X. Using thermal balance model to determine optimal reactor volume and insulation material needed in a laboratory-scale composting reactor. *Bioresour. Technol.* **2016**, *206*, 164–172. [[CrossRef](#)]
50. Ren, K.; Su, L.; Zhang, Y.; He, X.; Cai, X. Optimization and Experiment of Livestock and Poultry Manure Composting Equipment with Vented Heating. *Sustainability* **2023**, *15*, 11353. [[CrossRef](#)]
51. Ren, K.; Su, L.; Zhang, Y.; He, X.; Wu, H. Development and Evaluation of Cattle Dung Composting Equipment with Ventilation and Heating. *Appl. Sci.* **2023**, *13*, 8649. [[CrossRef](#)]

Disclaimer/Publisher’s Note: The statements, opinions and data contained in all publications are solely those of the individual author(s) and contributor(s) and not of MDPI and/or the editor(s). MDPI and/or the editor(s) disclaim responsibility for any injury to people or property resulting from any ideas, methods, instructions or products referred to in the content.